Rock Mechanics and Rock Engineering
https://doi.org/10.1007/s00603-025-04863-4

ORIGINAL PAPER

Two-Temperature Thermoporoelastic Modeling of Experimental Data for Wave Propagation in Glycerin-Saturated Tight Sandstones

Nianqi Li[1] · Li-Yun Fu[1,2] · José M. Carcione[3] · Wubing Deng[1,2]

Received: 2 February 2025 / Accepted: 4 August 2025

Abstract

Porous rocks in geothermal and ultradeep hydrocarbon reservoirs generally present large differences in temperature and thermal properties between the solid skeleton and pore fillings, leading to strong thermal coupling effects on the dissipation and attenuation of elastic waves, which remains unexplored theoretically. The theory of single-temperature thermoporoelasticity, as an extension of Biot poroelasticity by incorporating a single temperature (ST) and single-phase-lag (SPL)/dual-phase-lags (DPL) relaxation time of heat conduction, has been introduced in geophysics in recent years for wave propagation in non-isothermal porous rocks. However, the ST thermoporoelasticity assumes only an average temperature over the entire porous rock and becomes inadequate in describing the thermal relaxation of pore fillings and the thermal coupling due to heat transfer between the solid frame and pore fillings. We address this issue by proposing a two-temperature (TT) thermoporoelasticity with the DPL relaxation time of heat conduction, associated with analytical solutions and experimental verification. Plane wave analyses are performed for a comprehensive comparison of dispersion and attenuation between the TT-DPL, ST-DPL, and ST-SPL thermoporoelasticity models. The proposed TT-DPL model is used to interpret the laboratory measurements on a saturated sandstone with glycerin at different temperatures. It accounts for the effect of solid–fluid thermal expansion and shows larger thermal attenuation and velocity dispersion than the other two models. Ignoring the effect of solid–fluid thermal expansion when fitting the experimental data, however, leads to relatively high values of thermal conductivity and thermal relaxation time. The TT-DPL model provides a physically meaningful model for ultradeep hydrocarbon exploration, geothermal recovery, and other applications involving temperature variations between the solid frame and pore fillings.

Highlights

- Two-temperature thermoporoelasticity is proposed to describe the thermal coupling effect due to heat transfer between the solid frame and pore fillings in porous rocks.
- Plane-wave analyses compare various thermoporoelasticity models for dissipation and attenuation with/without the interphase coupling in saturated porous rocks.
- Experimental verification by a saturated sandstone with glycerin at different temperatures shows the significant effect of solid-fluid thermal coupling on attenuation and velocity dispersion.

Keywords Solid–fluid thermal expansion · Thermal expansion coefficients · Two-temperature thermoporoelasticity · Dual-phase-lags relaxation time

✉ Li-Yun Fu
lfu@upc.edu.cn

[1] State Key Laboratory of Deep Oil and Gas, China University of Petroleum (East China), Qingdao, China

[2] Laboratory for Marine Mineral Resources, Qingdao Marine Science and Technology Center, Qingdao, China

[3] National Institute of Oceanography and Applied Geophysics—INOGS, Trieste, Italy

Published online: 05 September 2025

1 Introduction

Classical thermoelasticity couples elastic deformation and heat flow (Biot 1956). The associated wave dissipation and attenuation are relevant to geophysical exploration (e.g., Treitel 1959; Savage 1966; Armstrong 1984) and earthquake seismology (e.g., Boschi 1973; Ritsema et al. 2011; Simmons et al. 2010). Particularly, the investigation of temperature-dependent wave propagation in fluid-filled porous rocks is of great interest for the exploration and development of geothermal and ultradeep hydrocarbon resources (e.g., Cermak et al. 1990; Jacquey et al. 2015; Fu 2017, 2019; Poletto et al. 2018; Chicco et al. 2019; Chicco and Mandrone 2022; Li et al. 2023; Cheng et al. 2024). Geothermal and ultradeep hydrocarbon reservoirs have been recognized as a thermoporoelastic medium involving complex thermal-liquid–solid coupling processes (e.g., Breede et al. 2013; Liu et al. 2018; Cui and Wong 2021; Jian et al. 2022; Wang et al. 2023) where the differences in temperature and thermal properties between the solid skeleton and pore fillings result in coupling effects that significantly influence wave dissipation and attenuation. In this study, we address this issue through theoretical modeling with confirmed validity.

Thermoporoelasticity (e.g., Noda 1990; Nield and Bejan 2006; Sharma 2008) is an extension of Biot poroelasticity by incorporating a single temperature (ST) and single-phase-lag (SPL) relaxation time of heat conduction (Lord and Shulman 1967) to couple elastic deformations with temperature and describe wave dissipation due to fluid and heat flows in porous media. Numerical simulations for wave propagation in ST-SPL thermoporoelastic media (Carcione et al. 2019) show that the thermal (T1) and Biot slow waves are diffusive at low frequencies and wave-like at high frequencies. Wei et al. (2020) formulated the Green function of ST-SPL thermoporoelasticity to investigate the effect of fluid viscosity and thermal properties on wave dissipation. The theory is extended to a double-porosity structure of pores and cracks (Kumar et al. 2017), but the resulting negative dissipation factors indicate instability. The problem is solved by incorporating the Biot–Rayleigh double-porosity theory (Ba et al. 2011), predicting positive dissipation factors (Li et al. 2022; Kumar et al. 2023). The resulting double-porosity thermoporoelastic model is then used to develop a coupled thermo-hydro-mechanical model (Li et al. 2023) for the cyclic recovery of fractured-vuggy thermal reservoirs. Yang et al. (2025) formulated an ST-SPL thermoacoustoelasticity for wave propagation in preheated and prestressed solid rocks. The refection and transmission (R/T) of inhomogeneous waves are investigated at the free surface of ST-SPL thermoporoelastic medium (Wang et al. 2021; Liu et al. 2022), at the interface between an elastic solid and ST-SPL thermoporoelastic medium (Kumar et al. 2022), and at the interface between two ST-SPL thermoporoelastic media (Hou et al. 2023). The resulting thermoporoelastic R/T model is applied to the seismic amplitude-variation-with-offset (AVO) modeling of Olkaria geothermal reservoirs for time-lapse reflection seismic monitoring (Cheng et al. 2024). However, these formulations based on the ST-SPL thermoporoelasticity assume only an average temperature over the entire fluid-filled rock and become inadequate in describing the thermal coupling effect of solid and fluid phases on the dissipation and attenuation of elastic waves.

It is worth mentioning that an ST thermoporoelasticity with a dual-phase-lags (DPL) relaxation time of heat conduction, which is proposed for metals (Tzou 1995; Chandrasekharaiah 1998), has been introduced for wave propagation in fluid-filled porous rocks (Liu et al. 2023; Kumar et al. 2024). The associated thermal relaxation effect is of relevance only in specialized applications involving very short time intervals and/or very large heat fluxes. Because of the most common engineering materials, such as metals, the value of relaxation time is known to be of the order of a picosecond or less. The ST-DPL thermoporoelasticity only accounts for such small thermal-relaxation effects caused by a very small difference of thermal properties between the pore infill (fluid) and frame. However, relevant experimental studies show that the relaxation times of different materials such as the rock frame and pore fluids are significantly different by the order of magnitude from second to a fraction of minute (Kaminski 1990; Vedavarz et al. 1992; Mitra et al. 1995). In addition, The ST-DPL thermoporoelasticity ignores the solid–fluid thermal coupling effect caused by heat transfer in different phases.

Thermal relaxation effects occurring in the solid phase of porous rocks are well recognized and described by the classical theory of thermoelasticity (e.g., Rudgers 1990; Carcione et al. 2018; Wang et al. 2020; Hou et al. 2021). Unlike the solid phase, the soft phase of porous rocks, such as pore fluids, kerogen, bitumen, and other organic matters, is more sensitive to temperature perturbations, presenting larger thermal relaxation effects. Noticeable changes in dispersion and attenuation due to the temperature-dependent physical properties in the soft phase have been observed (e.g., Batzle and Wang 1992; Nava et al. 1994; Schmitt 1999; Batzle et al. 2006; Han et al. 2008; Rabbani and Schmitt 2018; Yuan et al. 2019). The solid–fluid thermal coupling effect on the dissipation and attenuation of elastic waves enhances significantly with increasing temperature differences between solid and fluid phases. However, the theoretical understanding of these phenomena seems insufficient. Considering the temperature difference between the solid frame and the pore infill (fluid) of porous rocks for microscopic interactions in the heat transfer process, Youssef (2007) extended the ST-DPL theory to a two-temperature (TT) thermoporoelasticity with a dual-phase-lags model of heat conduction. It predicts

an additional slow thermal wave (T2) (Singh 2011). Hou et al. (2024) formulated the refection and transmission (R/T) of inhomogeneous waves at the interface between two TT-DPL thermoporoelastic media. However, these theoretical studies are lack of experimental data verification. In this study, we will address this issue by incorporating laboratory measurements.

As pointed out by Youssef (2007), there are two terms, $K(T_s–T_f)$ and $J\theta_s\theta_f$, that represent the temperature coupling effect in non-isothermal porous media where J is a mixed thermoelastic coupling coefficient. The former stands for the interphase heat transfer resulting from the unequal temperature of the phases at every point of the medium, which must be considered in application scenarios where the matrix temperature differs significantly from that in the surrounding fluid phase. Such significant temperature gradients are common in many situations such as thermal recovery, oil and gas drilling activities, and hydraulic fracturing (e.g., Breede et al. 2013; Olasolo et al. 2016). For example, large natural temperature gradients between hot thermal reservoir and cold recharge water in natural geothermal system have been recorded, which is due to the deep magma as source of heat (Banks 2012). On the other hand, thermal stresses occur when there is a temperature perturbation between the environment and the whole rock, regardless of whether there is an interphase temperature difference between the solid and fluid phases. The latter term is attributed to the differentiation of thermal expansion coefficients in different phases. Many experiments show that ignoring the solid–fluid thermal expansion leads to an incorrect interpretation of the thermo-osmotic experimental data and will result in higher values for thermal osmotic flow (e.g., Al-Bazali 2005; Roshan et al. 2015). Despite the fundamental importance of the heat transfer process between the solid and fluid phases which have been recognized, less literature has given a clear physical definition or specific values in plane wave calculations and numerical simulations. When the analytical solution including the correct effect of solid–fluid thermal expansion is used, no specific heat was needed to fit the experimental data for the rock samples. Ignoring the effect of solid–fluid thermal expansion in fitting the data, however, leads to unreasonably low, and incorrect, values for the specific heat coefficients. We refine the definition and unit of the aforementioned two coupling terms and corresponding coefficients in Sect. 2.2 as indicated in Table 1 for a saturated sandstone.

In this article, we start from the energy function in the Biot notation to formulate the constitutive and heat conduction equations of TT-DPL thermoporoelasticity in non-isothermal conditions. We use some empirical relations to characterize the temperature-dependent properties of the soft phase of porous rocks. Physical explanations to relevant thermoporoelastic coefficients in the TT-DPL model are provided in contrast to those in the ST-SPL model. The thermal coupling term due to the solid–fluid temperature difference cannot be neglected, given the inherent differences in the coefficient of thermal expansion that exist between the two phases. Further, we show that ignoring the solid–fluid thermal expansion leads to an incorrect interpretation of the seismic data and therefore erroneous estimation of the thermal properties. We use plane wave analyses to perform a comprehensive comparison of dispersion and attenuation between the TT-DPL, ST-DPL, and ST-SPL models. Finally, we use the TT-DPL model to interpret the laboratory measurements on the saturated sandstone with brine or glycerin (Yin et al. 2017) at different temperature. These findings provide an essential understanding of seismic exploration for reservoir characteristics under high-temperature conditions.

2 Methodologies

2.1 Equations of Motions

The theory of TT-DPL thermoporoelasticity emphasizes the differences in both temperature and thermal properties between the pore infill (fluid) and the frame in the heat transfer process. It includes the model parameters (four poroelastic moduli similar to Biot (1962) and seven additional coefficients without explicitly determined) in Eq. (30). Based on the double-temperature equations of heat conduction, we follow the ST-SPL thermoporoelasticity (Carcione et al. 2019) to redefine additional coefficients with a clear physical definition and units for investigating thermal interactions that occurs within and between the solid and fluid phases.

The displacement of the solid matrix and average fluid are designated by the components u_i and U_i, respectively, where t denotes the time variable and x_i, $i=1, 2, 3$ define the spatial variables. Moreover, we introduce the corresponding strain components:

$$e_{ij} = \frac{1}{2}\left(u_{i,j} + u_{j,i}\right) \text{ and } \epsilon = U_{i,i}, \tag{1}$$

and define the dilatations as $e=u_{i,i}$, where the subscript "$,i$" denotes the spatial derivative $\partial/\partial x_i$. The strain energy in thermoporoelasticity medium with two temperature items can be expanded as

$$\begin{aligned}\psi = {} & \mu e_{ij}e_{ij} + \frac{P}{2}e_{ii}e_{jj} + \frac{1}{2}R\epsilon^2 + Qe_{ii}\epsilon + Ce_{ii}\theta^{*s} \\ & + D_1 e_{ii}\theta^{*f} D_2\epsilon\theta^{*f} + F\epsilon\theta^{*s} + G\theta^{*s^2} + H\theta^{*f^2} + J\theta^{*s}\theta^{*f}.\end{aligned} \tag{2}$$

Compared with the original Eq. (30) in Youssef (2007), we amend temperature-related items from θ^m to θ^{*m}, where $\theta^{*m} = \theta^m/T_0$ and the supscript m ($m=s, f$) denote the solid and fluid phases, respectively, and θ^m is the temperature

Table 1 Physical properties of the material used in plane wave analysis

Properties	Values	
Grain bulk modulus, K_s (GPa)	35	
density, ρ_s (kg/m^3)	2650	
Frame bulk modulus, K_m (GPa)	1.7	
Shear modulus, μ_m (GPa)	1.8	
Porosity,ϕ	0.3	
Permeability, k (m^2)	1×10^{-15}	
Tortuosity,τ	2	
Fluid density, ρ_f (kg/m^3)	1000	
Viscosity, η (Pa·s)	0.001	
Thermoelastic coefficient, β_f (kg/(m·s^2·deg K))	40 000	
Bulk modulus, K_f (GPa)	2.40	
ST-SPL case in Carcione et al., 2017		
Bulk specific heat, C_V (kg/(m·s^2·degK))	Case 1 (rock)	Case 2 (gas)
	1.8×10^6	1000
Thermoelastic coefficient, β (kg/(m·s^2·degK))	120 000	
Thermal conductivity, k (m·kg/(s^3·degK))	10.5	
Relaxation time, τ (s)	1.5×10^{-8}	
TT-DPL case in this work		
Solid specific heat, C_E^s (kg/(m·s^2·degK))	Case 1 (rock)	Case 2 (gas)
	1.08×10^6	754
Thermal expansion coefficient, α_s (degK^{-1})	1.3×10^{-6}	
Thermal conductivity, k_s (m·kg/(s^3·degK))	14.7	
Relaxation time, τ_f (s)	1.5×10^{-8}	
Fluid specific heat, C_E^f(kg/(m·s^2·degK))	3.5×10^6	4186
Thermal expansion coefficient, α_f (degK^{-1})	3.8×10^{-4}	
Thermal conductivity, k_f (m·kg/(s^3·degK))	0.61	
Relaxation time, τ_f (s)	1.5×10^{-8}	
Solid–fluid thermal expansion coefficient,$\alpha_{sf}=\alpha_{fs}$ (degK^{-1})	2×10^{-5}	

perturbation above a reference absolute temperature T_0 of the phases. We also use the notation P in Eq. (2) replacing the original notation λ in Youssef's (2007) Eq. (29), since μ and λ commonly represent the Lamé constants. In addition to the poroelastic moduli R, Q consistent with Biot (1962), the parameters C, D_1, D_2, F, G, H, and J are interpreted only as additional mixed and thermal coefficients, lacking a clear physical definition or unit. We give the definitions and expressions for the seven parameters in Appendix A, which can be determined as a function of the solid and fluid and the microstructural properties of the medium. Note the temperture coupling term between the solid and the fluid represented by the coefficient J.

Based on the heat transfer in the solid and fluid (Youssef 2007), the thermal expansion coefficient of both phases can be introduced to include the inertial and the nonlinear advection terms in the two-temperature equation. The extending law of TT is

$$k^s\theta^s_{,ii}=\left(\frac{\partial}{\partial t}+\tau_0^s\frac{\partial^2}{\partial t^2}\right)\left(\rho C_E^s\theta^s-\left(3\alpha_s\beta_{sf}+\alpha_{fs}\beta_f\right)T_0^s\theta^f+T_0^s\beta_s e_{ii}+T_0^s\beta_{fs}\epsilon\right)+h\left(\theta^s-\theta^f\right), \tag{3}$$

$$k^f\theta^f_{,ii}=\left(\frac{\partial}{\partial t}+\tau_0^f\frac{\partial^2}{\partial t^2}\right)\left(\rho C_E^f\theta^f-\left(3\alpha_{sf}\beta_s+\alpha_f\beta_{fs}\right)T_0^f\theta^s+T_0^f\beta_{sf}e_{ii}+T_0^f\beta_f\epsilon\right)+h\left(\theta^f-\theta^s\right), \tag{4}$$

where the coefficient of heat conduction (or thermal conductivity) k, the increment of temperature θ above a reference

absolute temperature T_0 for the state of zero stress and strain, the specific heat capacity C_E, the relaxation time τ_0, and the thermoelasticity coefficient β are common thermoelastic parameters. The superscript '*s*' and '*f*' represent the solid and liquid phases, respectively, while the superscripts '*sf*' and '*fs*' indicate the coupling between the phases. h is the interphase heat transfer coefficient, kg/(s^3·degK), and other properties are given in Appendix A (Eqs. 27 and 28).

Since we assume that the temperatures of the skeleton and the fluid are locally the same, the coupling terms of interphase heat convection $h(\theta^f - \theta^s)$ resulting from the unequal temperature of the phases can be neglected. However, this item should not be ignored in special application scenarios, e.g., the cyclic recovery of thermal reservoirs and cold shock on dry hot rocks. τ is the relaxation time. In classical thermoporoelastic theory, τ_0 is used as the equivalent relaxation time by neglecting the differences between the two phases. However, studies on various materials have shown that the difference in thermal relaxation time between solid and liquid can reach several orders of magnitude at room temperature (e.g., Kaminski 1990; Mitra et al. 1995). Following Youssef's (2007) study, we introduce two relaxation times (τ_0^s and τ_0^f) into heat conduction equations, which avoids the overestimation of thermal effects on wave dissipation and the two relaxation times involved become more distinct in physics.

Since Eqs. (3) and (4) involve only the volumetric strain and do not introduce shear strain, the shear wave is not affected by temperature under the TT theoretical framework. Effective stress and effective pressure play an important role in rock physics. The total stress is decomposed into an effective stress, which acts on the frame, and into a hydrostatic stress, which acts on the fluid. As shown by Carcione et al. (2019), the constitutive relation of thermoporoelasticity theory with single temperature for the frame σ_{ij} and fluid σ_f is

$$\sigma_{ij} = 2\mu e_{ij} + \big((\lambda + \alpha^2 M)e + \alpha M w - \beta\theta\big)\delta_{ij}, \tag{5}$$

$$\sigma_f = \alpha\phi M e + \phi M w - \beta_f \theta, \tag{6}$$

where the macroscopic particle velocity of the fluid relative to the solid is $w = \phi(U_{i,i} - u_{i,i})$. λ is the Lamé constant of the drained matrix and μ is the shear modulus of the drained (and saturated) matrix. α and M are the stiffness coefficients given in Appendix A. If thermal interaction within and between the solid and fluid phases are considered, as in Carcione et al. (2019), we have the extended constitutive relations:

$$\begin{aligned}\sigma_{ij} = {} & 2\mu e_{ij} + \lambda e_{kk}\delta_{ij} + \alpha M(\alpha e + w)\delta_{ij} \\ & - \big[\big(3K_m + 3\alpha M(\alpha - \phi)\big)\alpha_s + \alpha\phi M\alpha_{fs}\big]\theta^s\delta_{ij} \\ & - \big[\big(3K_m + 3\alpha M(\alpha - \phi)\big)\alpha_f + \alpha\phi M\alpha_{sf}\big]\theta^f\delta_{ij}\end{aligned} \tag{7}$$

$$\begin{aligned}\sigma_f = {} & \phi\alpha M e + \phi M w - \big(\alpha_f\phi M + 3\alpha_{sf}M(\alpha - \phi)\big)\theta^f \\ & - \big(\alpha_{fs}\phi M + 3\alpha_s M(\alpha - \phi)\big)\theta^s.\end{aligned} \tag{8}$$

The dynamical equations are

$$\begin{cases} \sigma_{ij,j} = \rho\ddot{u}_i + \rho_f\ddot{w}_i, \\ \sigma_{f,i} = \phi\rho_f\ddot{u}_i + \chi\rho_f\ddot{w}_i + \phi\eta/\kappa\dot{w}_i, \end{cases} \tag{9}$$

where the quantity $\rho = (1-\phi)\rho_s + \phi\rho_f$ is the composite density with solid ρ_s and fluid phase ρ_f. χ is the tortuosity and the Darcy law defines the movement of viscous fluids of viscosity η in the frame of permeability κ.

Coupling the TT heat conduction equation (Eqs. 3 and 4) and the constitutive relation (Eqs. 7 and 8) into momentum conservation (Eq. 9), the non-isothermal wave equations for isotropic thermoporous medium with two relaxation times are

$$\begin{cases} \mu u_{i,jj} + (\lambda + \mu + \alpha^2 M)u_{j,ij} + \alpha M w_{j,ij} - \big[\big(3K_m + 3\alpha M(\alpha - \phi)\big)\alpha_s + \alpha\phi M\alpha_{fs}\big]\theta^s_{,i} - \big[\big(3K_m + 3\alpha M(\alpha - \phi)\big)\alpha_f + \alpha\phi M\alpha_{sf}\big]\theta^f_{,i} = \rho\ddot{u}_i + \rho_f\ddot{w}_i, \\ \phi\alpha M u_{j,ij} + \phi M w_{j,ij} - (\alpha_{fs}\phi M + 3\alpha_s M(\alpha - \phi))\theta^s_{,i} - \big(\alpha_f\phi M + 3\alpha_{sf}M(\alpha - \phi)\big)\theta^f_{,i} = \phi\rho_f\ddot{u}_i + \chi\rho_f\ddot{w}_i + \phi\eta/\kappa\dot{w}_i, \\ k^s\theta^s_{,ii} = \Big(\frac{\partial}{\partial t} + \tau_0^s\frac{\partial^2}{\partial t^2}\Big)\Big(\rho C_E^s\theta^s - (3\alpha_s\beta_{sf} + \alpha_{fs}\beta_f)T_0^s\theta^f + T_0^s(\beta_s + \beta_{fs})e_{ii} + \frac{T_0^s\beta_{fs}}{\phi}w\Big) \\ k^f\theta^f_{,ii} = \Big(\frac{\partial}{\partial t} + \tau_0^f\frac{\partial^2}{\partial t^2}\Big)\Big(\rho C_E^f\theta^f - (3\alpha_{sf}\beta_s + \alpha_f\beta_{fs})T_0^f\theta^s + T_0^f(\beta_{sf} + \beta_f)e_{ii} + \frac{T_0^f\beta_f}{\phi}w\Big). \end{cases} \tag{10}$$

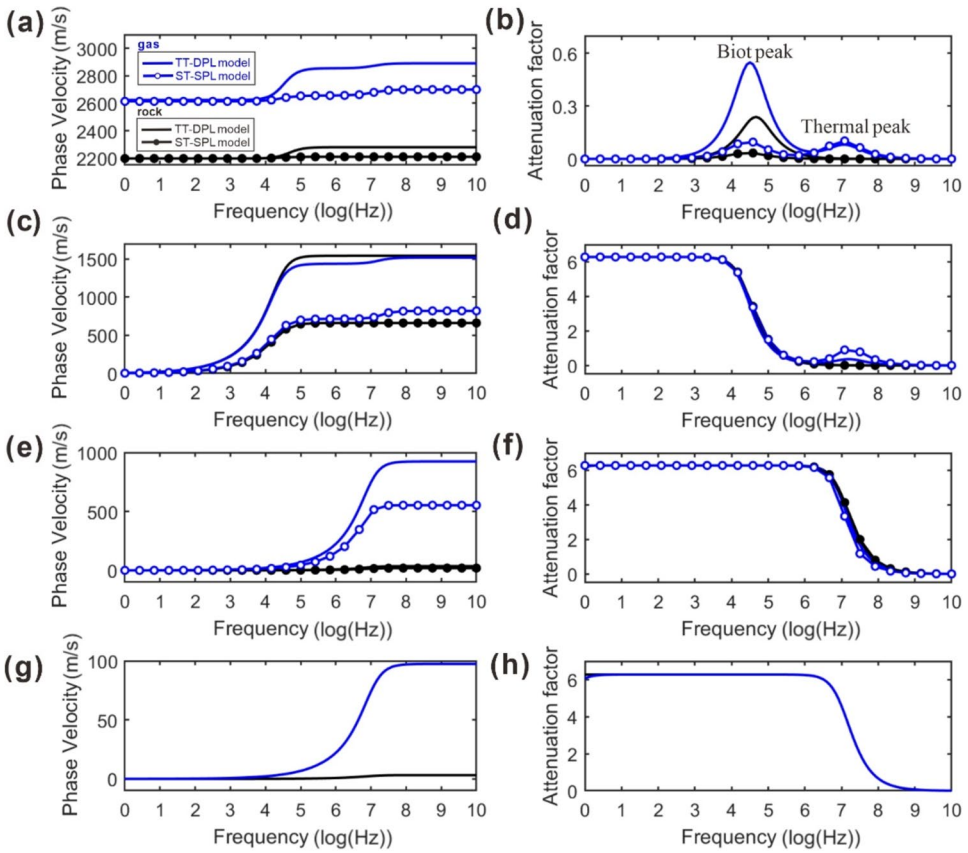

Fig. 1 **a**, **c**, **e** and **g** Phase velocity and **b**, **d**, **f** and **h** attenuation as a function of frequency for **a** and **b** fast P wave, **c** and **d** slow Biot wave, **e** and **f** thermal wave (T1), and **g** and **h** thermal wave (T2) in different models, where the black and blue lines correspond to a rock and pure gas regarding the constant specific heat, respectively. The P wave velocity predicted by the ST-SPL model (Carcione 2007, Fig. 7.31) approaches that of the TT-DPL model at low frequencies. The properties are listed in Table 1

If we neglect the thermal coupling effect between the solid–fluid phases, but include the thermal term within each phase and set $\theta^s = \theta^f$, we have $\beta = \beta_s + \alpha\beta_f$, and Eqs. (7) and (8) reduce to the classical thermoporoelasticity equations. If thermoelastic coupling coefficients $J = 3\alpha_s\beta_{sf} + \alpha_{fs}\beta_f = 0$, we can combine the temperature perturbation terms of the solid and fluid at $\theta^s = \theta^f = \theta$ as discussed in Appendix B. Equations (3) and (4) reduce to heat conduction equation for a single temperature. Equation 10 reduces to the thermoporoelasticity equation (Carcione et al. 2019):

$$\begin{cases} \mu u_{i,jj} + \left(\lambda + \mu + \alpha^2 M\right) u_{j,ij} + \alpha M w_{j,ij} + \beta\theta_{,i} = \rho\ddot{u}_i + \rho_f \ddot{w}_i, \\ \phi\alpha M u_{j,ij} + \phi M w_{j,ij} - \beta_f \theta_{,i} = \phi\rho_f \ddot{u}_i + \chi\rho_f \ddot{w}_i + \phi\eta/\kappa\dot{w}_i, \\ kT_{,i,i} = \rho C_e\left(\dot{\theta} + \tau_0\ddot{\theta}\right) + T_0\beta\left(\dot{u}_{i,i} + \tau_0\ddot{u}_{i,i} + \dot{w}_i + \tau_0\ddot{w}_i\right). \end{cases} \tag{11}$$

However, the values of α_s and α_f are usually observed in the order of 10^{-6} to 10^{-5} K^{-1} and 10^{-4} K^{-1}, respectively (Robertson 1988; Roshan et al. 2015). Therefore, we can estimate the order of magnitude of the terms $36Q^2\alpha_s\alpha_f$ (around 10^9) larger than the terms $9P^2\alpha_s^2 + 6PR\alpha_s\alpha_f + R^2\alpha_f^2$ (around 10^8), so the solid–fluid thermal expansion coefficient α_{sf} has no real root when $J = 0$. Only when the thermal expansion coefficients of two phase are very close (on the same order of magnitude), α_{sf} has a real solution and thermoelastic coupling terms can be neglected. This is consistent with many experiments, and analyzing the results ignoring the solid–fluid thermal expansion leads to an incorrect interpretation of the thermo-osmotic experimental data and will result in higher values for thermal osmotic flow (e.g., Al-Bazali 2005; Roshan et al. 2015).

2.2 Plane Wave Analysis

If temperature perturbation q and displacement field u_i are the fundamental variables $\mathbf{u}_i \equiv \left(\, u_i \;\; w_i \;\; \theta^s \;\; \theta^f \,\right)^\dagger$ of the thermoelastic medium shown in Eq. (9), then after some manipulations, we obtain the following matrix form for Eq. (10):

$$\boldsymbol{\rho}\ddot{\mathbf{u}}_i = -\mathbf{d}\dot{\mathbf{u}}_i + \partial_j\left(\mathbf{K}\boldsymbol{\Delta}\delta_{ij} + 2\boldsymbol{\mu}\tilde{\boldsymbol{\varepsilon}}_{ij} + \mathbf{A}\dot{\mathbf{u}}_i + \mathbf{B}\ddot{\mathbf{u}}_i + \mathbf{C}\mathbf{u}_i\delta_{ij}\right). \tag{12}$$

For the DT-DPL thermoelasticity, the matrices **r**, **d**, **m**, **K**, **A**, **B**, and**C** are defined as

$$
\mathbf{\rho} \equiv \begin{pmatrix} \rho & \rho_f & 0 & 0 \\ \phi\rho_f & \chi\rho_f & 0 & 0 \\ 0 & 0 & \tau_0^s \rho C_E^s & 0 \\ 0 & 0 & 0 & \tau_0^f \rho C_E^f \end{pmatrix}, \quad \mathbf{d} \equiv \begin{bmatrix} 0 & 0 & 0 & 0 \\ 0 & \phi\frac{\eta}{\kappa} & 0 & 0 \\ 0 & 0 & \rho C_E^s & 0 \\ 0 & 0 & 0 & \rho C_E^f \end{bmatrix}, \quad \mathbf{\mu} \equiv \begin{bmatrix} \mu & 0 & 0 & 0 \\ 0 & 0 & 0 & 0 \\ 0 & 0 & 0 & 0 \\ 0 & 0 & 0 & 0 \end{bmatrix}, \quad \mathbf{K} \equiv \begin{bmatrix} \lambda+\mu+\alpha^2 M & \alpha M & 0 & 0 \\ \phi\alpha M & \phi M & 0 & 0 \\ 0 & 0 & k^s & 0 \\ 0 & 0 & 0 & k^f \end{bmatrix},
$$

$$
\mathbf{A} \equiv \begin{bmatrix} 0 & 0 & 0 & 0 \\ 0 & 0 & 0 & 0 \\ T_0(\beta_s+\beta_{fs}) & \frac{T_0\beta_{fs}}{\phi} & 0 & 0 \\ T_0(\beta_{sf}+\beta_f) & \frac{T_0\beta_f}{\phi} & 0 & 0 \end{bmatrix}, \quad \mathbf{B} \equiv \begin{bmatrix} 0 & 0 & 0 & 0 \\ 0 & 0 & 0 & 0 \\ \tau_0^s T_0(\beta_s+\beta_{fs}) & \frac{\tau_0^s T_0\beta_{fs}}{\phi} & 0 & 0 \\ \tau_0^f T_0(\beta_{sf}+\beta_f) & \frac{\tau_0^f T_0\beta_f}{\phi} & 0 & 0 \end{bmatrix}, \tag{13}
$$

$$
\mathbf{C} \equiv \begin{bmatrix} 0 & 0 & -(3K_m+3\alpha M(\alpha-\phi))\alpha_s - \alpha\phi M\alpha_{fs} & -(3K_m+3\alpha M(\alpha-\phi))\alpha_f - \alpha\phi M\alpha_{sf} \\ 0 & 0 & -\alpha_{fs}\phi M - 3\alpha_s M(\alpha-\phi) & -\alpha_f\phi M - 3\alpha_{sf} M(\alpha-\phi) \\ 0 & 0 & 0 & 0 \\ 0 & 0 & 0 & 0 \end{bmatrix}.
$$

We consider a harmonic plane P or linearly polarized S wave in a homogeneous, isotropic medium to investigate the frequency dependence of phase velocity and attenuation. In this case, let us denote the dependency of $\mathbf{u}$ on time t and the position x by $\mathbf{u} = \mathbf{\upsilon}\exp(-i\omega t + ik^* x)$, where w is the angular frequency, $\mathbf{u}$ is the displacement amplitudes within the wave, $k^* \equiv k_{\mathrm{re}} + ik_{\mathrm{im}}$ is the complex wavenumber, k_{re} is the ordinary wavenumber, and k_{im} is the spatial attenuation coefficient for the wave. Since the thermoporoelastic models and TT-DPL models are formulated under the same general matrix notation, plugging the harmonic wave into Eq. (11) and denoting $\gamma \equiv k^{*2}/\omega^2$, we obtain a generalized eigenvalue problem for $k.^*$ and $\mathbf{u}$ (similar to Morozov and Deng 2016):

$$
\mathbf{\rho}^*\mathbf{\upsilon} = \Upsilon^2\mathbf{M}^*\mathbf{\upsilon} + \Upsilon\mathbf{N}^*\mathbf{\upsilon}, \tag{14}
$$

where $\mathbf{\rho}^* \equiv \mathbf{\rho} + i\mathbf{d}/\omega$ is the complex-valued density matrix. For P wave modes, the matrices $\mathbf{M}^* \equiv \mathbf{K} + 4/3\mathbf{\mu}$ and $\mathbf{N}^* \equiv -\mathbf{A} + i\omega\mathbf{B} - i\omega^{-1}\mathbf{C}$, but for shear wave, $\mathbf{M}^* \equiv \mathbf{\mu}$ and $\mathbf{N}^* \equiv 0$, where the material property matrices $\mathbf{r}$, $\mathbf{d}$, $\mathbf{K}$, $\mathbf{m}$ in the equation are all real valued, and the shear wave is affected by neither pore fluids nor temperature variations. The resulting eigenvalues of Eq. (14) are yielded by the relation $\Upsilon^2 \equiv k^{*2}/\omega^2 \equiv \left(k_{\mathrm{re}} + ik_{\mathrm{im}}\right)^2/\omega^2$. The number of eigenvalues equals the number of variables in model parameterization. For each wave mode, the phase velocity dispersion V_{phase} and the attenuation spectrum Q^{-1} are given, respectively, by

$$
\begin{cases} V_{\mathrm{phase}} \equiv \dfrac{\omega}{k_{\mathrm{re}}} = \dfrac{1}{\mathrm{Re}\Upsilon} \\ Q^{-1} = \dfrac{\mathrm{Im}\Upsilon}{2\mathrm{Re}\Upsilon} \end{cases}. \tag{15}
$$

Equation (14) is a quadratic eigenvalue problem, which can be solved by using various numerical methods.

3 Results and Discussion

3.1 Examples

We compare the ST-SPL and TT-DPL thermoporoelasticity theories with the material properties given in Table 7.1 of Carcione (2007). We assume two values of the bulk (volumetric) specific heat. Figure 2 illustrates the variations in elastic wave velocity and dispersion under conditions of differing solid–fluid temperatures, which are relevant to practical engineering scenarios such as thermal recovery of heavy oil and geothermal energy extraction. Figures 3, 4, 5 and 6 show different sets of thermophysical properties (α_k, and τ_0^k, $k{=}s, f$) to highlight the thermal coupling between the solid and the fluid, which avoids the overestimation of thermal effects on wave dissipation and two lagging times involved become more distinct in physics.

Figure 1 shows the phase velocities of the four wave modes (a) and attenuation factor of the fast P wave as a function of frequency, where the black and blue lines correspond to real rock and idealized material with prominent thermal effects, respectively. In both the ST-SPL and TT-DPL models, the Biot and thermal relaxation peaks can be observed at high frequencies. In rocks, the thermal (T) wave loss is very weak, and the Biot peak dominates the attenuation. The two peaks are comparable in intensity in the case of gas, and the heat flow contributes to the fast P wave attenuation.

Figure 1 compares the results to those of Carcione 's (2007) ST-SPL model (blue line in Fig. 1, ignoring the solid-flow thermal expansion difference, $\alpha_{sf} = 0$). We see that the proposed TT-DPL theory predicts two P waves and two T waves. Attenuation in the seismic band can be more significant due to fast P wave to thermal mode conversion in heterogeneous media considering solid–fluid coupled thermal effects, which can be termed wave-induced thermoporoelastic attenuation in analogy with wave-induced fluid-flow

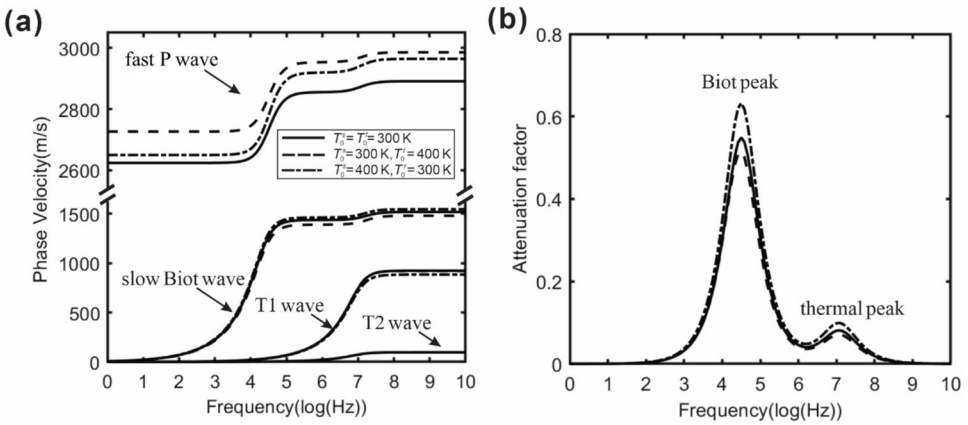

Fig. 2 The phase velocities of the three wave modes (**a**) and the attenuation factor (b) of the fast P wave as functions of frequency, with the solid, dashed, and dotted–dashed lines corresponding to the isothermal case, the higher-temperature contents case, and the higher-temperature background matrix case, respectively. The properties are listed in Table 1

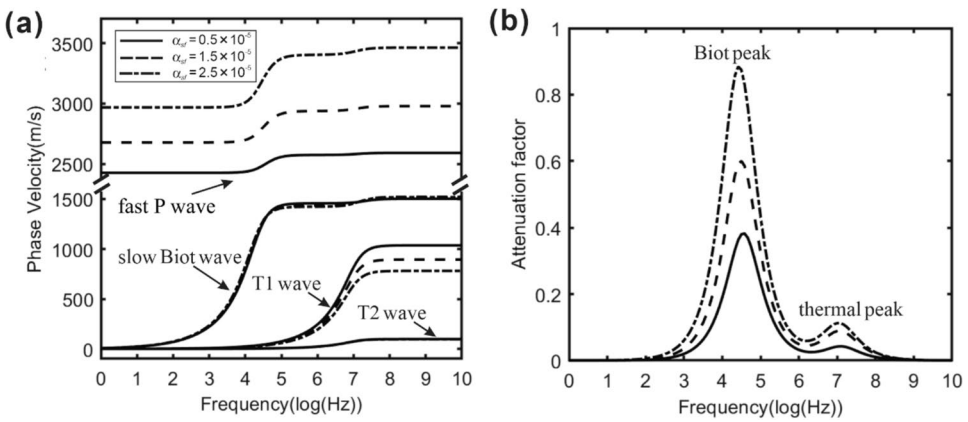

Fig. 3 The phase velocities of the three wave modes (**a**) and the attenuation factor (b) of the fast P wave as functions of frequency for different solid–fluid thermal expansion coefficients. The properties are listed in Table 1

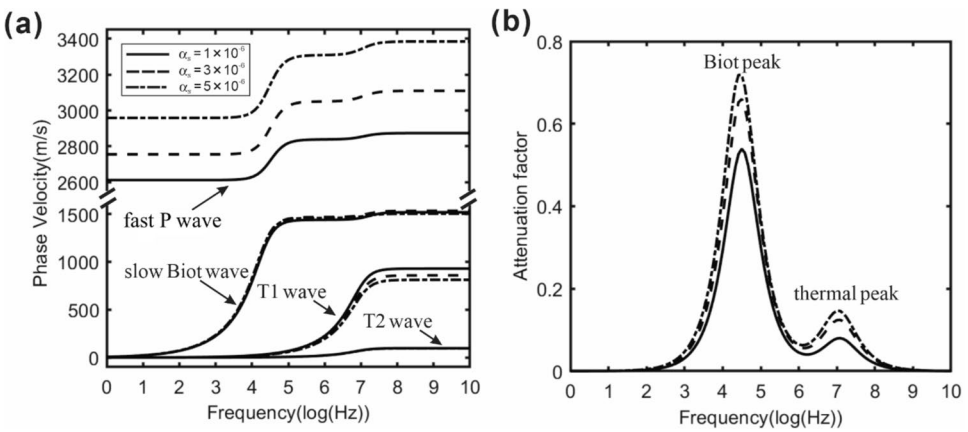

Fig. 4 The phase velocities of the three wave modes (**a**) and the attenuation factor (b) of the fast P wave as functions of frequency for different solid thermal expansion coefficients. The properties are listed in Table 1

(mesoscopic) attenuation related to the Biot slow mode. The dispersion curve of the fast P wave has two inflection points, namely two attenuation peaks in Fig. 1b. The stronger attenuation peak appears at seismic frequencies ($10^4 \sim 10^5$ Hz) showing the effect of Biot's friction (Biot 1962). The ultrasonic frequencies ($10^6 \sim 10^7$ Hz) correspond to the thermal attenuation. Physically, the slow Biot wave represents global or macroscopic flow of fluid driven by pressure in porous media, whereas the thermal wave (T mode) reflects the propagation of global or macroscopic thermal diffusion related to heat. It is the differences in both temperature and thermal diffusion properties between the two phases, as pointed out by the TT-DPL theory, that cause the T mode to split into the T1 wave and T2 wave. The T1 wave is a global thermal diffusion propagation with relatively high speed, whereas the T2 wave is an extremely slow local thermal diffusion propagation in the fluid phase.

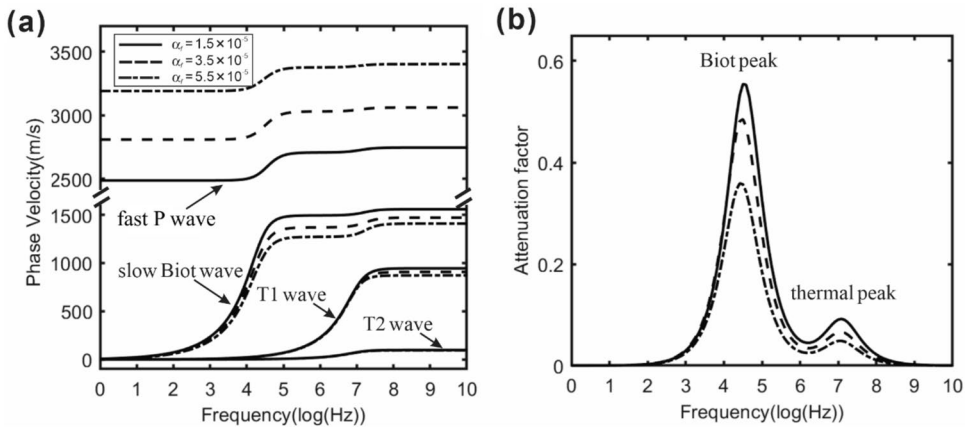

Fig. 5 The phase velocities of the three wave modes (**a**) and the attenuation factor (b) of the fast P wave as functions of frequency for different fluid thermal expansion coefficients. The properties are listed in Table 1

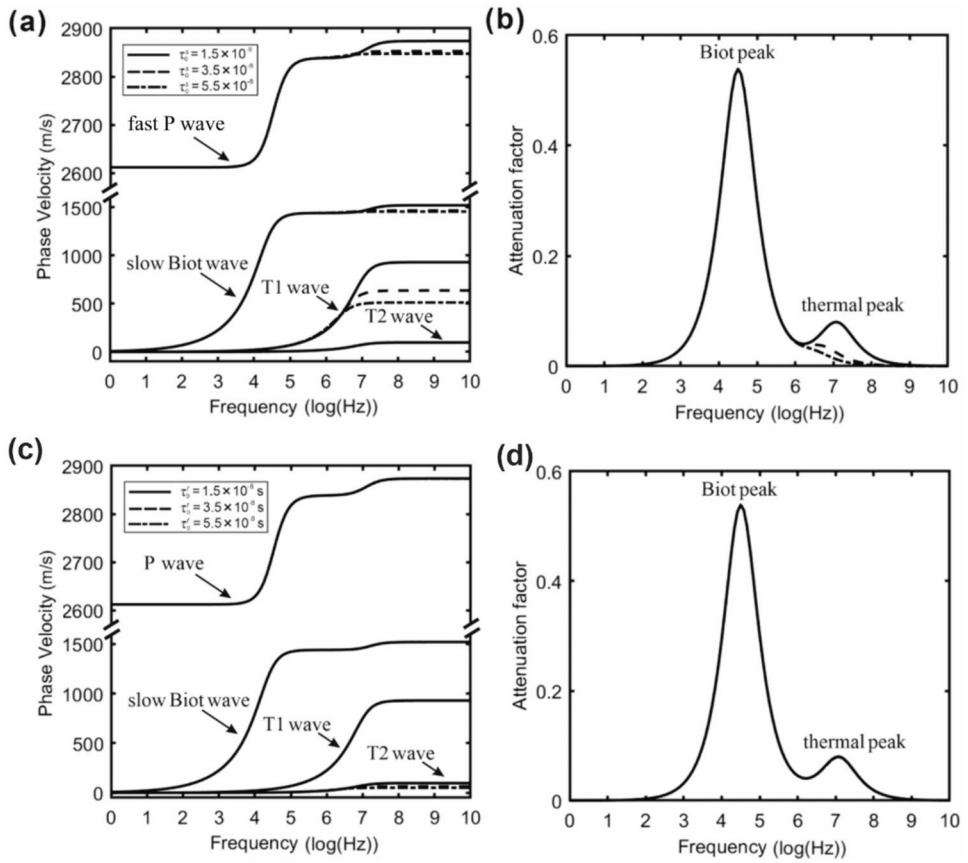

Fig. 6 The phase velocities of the three wave modes and the attenuation factor of the fast P wave as functions of frequency for different solid relaxation times (**a**, **b**) and fluid relaxation times (**c**, **d**). The properties are listed in Table 1

The difference in temperature (Fig. 2) and thermal properties (Figs. 3, 4, 5 and 6) between the pore infill (fluid) and the frame should be considered for microscopic space interactions in the heat transfer process. The propagation characteristics of elastic waves in porous media are usually affected by the temperature difference effect between the rock matrix and fluid, such as geothermal reservoir rocks experiencing a cold- shock treatment for thermal recovery (e.g., Breede et al. 2013; Olasolo et al. 2016) and altering the viscosity through heating the fluid to enhance heavy oil recovery (Spencer 2013), leading to a non-isothermal state generally. Therefore, we investigate the dispersion and attenuation properties with different temperature combinations (Case 1: $T_0^s = T_0^f = 300$ ºK, Case 2: $T_0^s = 300$ ºK, $T_0^f = 400$ ºK, and Case 3: $T_0^s = 400$ ºK, $T_0^f = 300$ ºK). Figure 2 compares the isothermal state (Case 1) to non-isothermal results (Cases 2 and 3); the minimum longitudinal wave velocity shown in Case 1 may due to the lowest average temperature. Notably, when the cold fluid impacts the hot

rock matrix (Case 3), a more pronounced increase in the Biot attenuation peak is observed in Fig. 2b. The slow Biot wave velocity is slightly higher and the T1 wave velocity slightly lower than the other two cases.

There are rarely discussions on the solid–fluid coupling thermal expansion effects in the published literature. The (1) complex physical and chemical interactions that may occur between the two-phase medium under variations in temperature and pressure, and (2) the difficulty in obtaining directly data from laboratory experiments, have resulted in limited attention being given to this issue. It is well known that differences in thermal expansion between mineral particles in rocks can generate thermal stress (e.g., Richter and Simmons 1974; Wong and Brace 1979; Ma et al. 2021), and the disparity in thermal expansion coefficients between solids and fluids further influences fluid flow, wave propagation, and the mechanical behavior of the medium within the pore structure. During seismic wave propagation, especially in water-saturated geotechnical media, the thermal effects induced by seismic waves may cause localized temperature increases and thermal expansion differences, which in turn alter the propagation path and velocity of the waves, significantly affecting the attenuation characteristics of the seismic waves and the medium's response behavior. As shown in Fig. 3a, the fast P wave and T wave velocities significantly increase by increasing coupled thermal expansion coefficients. The Biot attenuation peak is significantly affected by the high α_{sf} and the thermal wave attenuation peak slightly increases (Fig. 1b). Therefore, the effect of coupled thermal expansion coefficients on the T2 waves are not significant. Interestingly, the T1 wave shows decreasing phase velocity with increasing coupled thermal expansion coefficients, i.e., an opposite trend compared to that of the fast P wave mode.

The differential thermal expansion of different mineral and fluid phases is another critical parameter in temperature-induced velocity variations. In particular, different phases produce differential thermal stresses due to uncoordinated deformations. Figures 4 and 5 show the frequency-dependent phase velocities and attenuation factors of fast P, slow Biot, and thermal T1 and T2 waves with different thermal expansion coefficients of solid and fluid, respectively. Figures 4a and 5a demonstrate that as the thermal expansion coefficients increase, the fast P wave velocity consistently increases, whereas the corresponding attenuation exhibits an opposite trend in Figs. 4b and 5b. As the solid thermal expansion coefficient increases, the Biot and thermal attenuation peaks show a slight increase, while the slow Biot wave and two thermal wave attenuation peaks remain almost unaffected. In contrast, Fig. 5 shows that the fast P wave attenuation significantly decreases and slow Biot wave attenuation increases with the increasing fluid thermal expansion coefficient. Although the liquid phase occupies a smaller proportion compared to the solid phase in saturated rocks, Fig. 5 demonstrates that the fluid's effect on wave velocity dispersion and attenuation is significant under different thermal expansion coefficients. This is consistent with the observed phenomenon in laboratory experiments, where wave velocity and dispersion in rocks saturated with fluids of different thermal expansion coefficients show notable differences (Yin et al. 2017). This also contributes to advancing the understanding of subsurface fluid monitoring and fluid identification (Tura and Lumley 1998).

Two lagging times are involved in the transient process. For the ST-DPL thermoporoelastic model (Tzou 1995; Chandrasekharaiah 1998; Liu et al. 2023), thermal energy is mainly transmitted into the frame with the heat flux lagging time representing a macroscopic average time delay in this process (Tzou, 2014), whereas the temperature gradient lagging time is interpreted as the delay time caused by the microstructural interactions in microscale or small-scale effects of heat transport in space. Different from ST-SPL, we follow Youssef's (2007) to define two lagging times as the time required for the temperature of the solid and fluid components to adjust and reach thermal equilibrium after an external temperature disturbance. Figures 6 show the effect of two different relaxation times on individual wave modes compared with the same relaxation times ($\tau_0^s = \tau_0^s = 1.5 \times 10^{-8}$ s) model . Figures 6 show the fast P dispersion and the corresponding Biot attenuation remain unchanged though thermal attenuation slightly decrease compare with the same relaxation times case. The value of the two relaxation times and their difference are negatively correlated with phase velocity and attenuation peak. The slow Biot and thermal T1 waves exhibit a decreasing trend with increasing solid relaxation time, similar to the fast P

Table 2 Thermophysical properties of minerals and cements of common sandstones at room temperature and pressure

Component	$\alpha(\times 10^{-6}$ /K)			c ($\times 10^6$ kg/(m s^2 K))	k (m kg/(s^3 K))
Quartz	13.6	–	7.4[a]	2.0[e]	7 ~ 12[e]
Potassium feldspar	5.33	2.67	4[b]	2.5[e]	1.4 ~ 2[e]
Albite	11.25	3.75	3.75[c]	2.2[e]	2 ~ 2.4[e]
Calcite	−5.5	25.37	–[d]	2.3[e]	3.5 ~ 4[e]
Muscovite	9.94	11.1	13.79[d]	2.3[e]	4.05[g]
Biotite	5	–	–[d]	2.4[f]	3.7[g]
Clays	10	–	–[e]	1.6[e]	2.2[e]

[a]Kirby (1969)

[b]Skinner (1966)

[c]Huotari and Kukkonen (2004)

[d]Clarke (1928)

[e]Robertson (1988)

[f]Oetting and Holley (1982)

[g]Gray and Uher (1977)

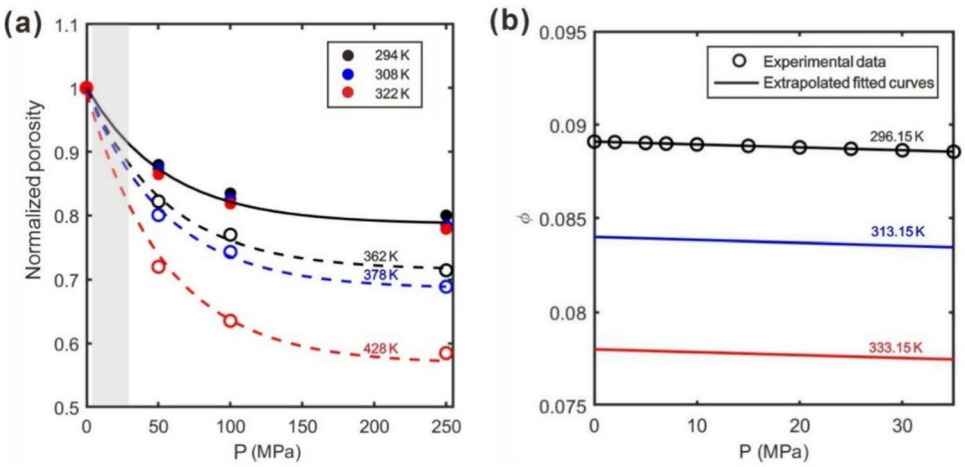

Fig. 7 **a** Impact of temperature on pressure-dependent porosity properties in saturated sandstone samples (Abdulagatova et al. 2010), where the solid black line indicates that he porosity follows the same trend of change within the temperature range below 362 K. **b** Experimental data (Yin et al. 2017; hollow black circles) and the extrapolated pressure-dependent porosity at 296.15 K (black line), 313.15 K (blue line), and 333.15 K (red line) used in the model prediction

wave in Fig. 6a. In contrast, as shown in Fig. 6c, the fluid relaxation time only affects the thermal T2 wave.

3.2 Interpretation of Laboratory Measurements

Significant temperature gradients in porous media reservoirs are encountered in many situations such as oil and gas drilling activities, geothermal recovery, or unconventional resources exploration (Soler 2001; Fu 2017; Chicco and Mandrone 2022). Despite that the influence of temperature changes on the pore structure of the matrix and the properties of the fluids has been extensively reported, the importance of the solid–fluid thermal coupling process has had very little attention in the past, especially in saturated porous media under varying pressure and temperature conditions. In this section, we validate the TT-DPL model using the experimental data on velocity dispersion in glycerol-saturated sandstone by Yin et al. (2017), and invert the coupled thermal expansion coefficient. The selected experimental data (circled in Fig. 9(a)) includes the following measurement parameters: ultrasonic frequency of 1 MHz, three different temperatures (296.15 K, 313.15 K, and 333.15 K), and measurement effective pressure ranging from 2 to 35 MPa. As shown in Table 2, most of the rock physical property parameters of the sample can be obtained directly or indirectly from the charts and measurement data provided by Yin et al. (2017), but thermal physical property parameters are lacking. Additionally, we note that the pressure-dependent porosity (circled in Fig. 7b) provided by Yin et al. (2017) does not account for temperature effects, given that the selected experimental data involve relatively different temperatures, which is likely to influence the porosity. As shown in Fig. 7a, the normalized trend of pressure-dependent porosity of several saturated samples measured by Abdulagatova et al. (2010) indicates that the porosity follows the same trend of change within the temperature range below 362 K. The value of porosity variation with temperature has been reported to range from 0.0001 K^{-1} to 0.0007 K^{-1} for temperatures below 362 K (Cheng et al. 1990; Maqsood and Kamran 2005; Abdulagatova et al. 2010; Sirdesai et al. 2018). We assume it to be a constant value of 0.0003 K^{-1}, while the temperature- and pressure-dependent porosity properties of glycerol-saturated sandstone samples are shown in Fig. 7(b).

As indicated by Yin et al. (2017), the sample from the northeastern Sichuan basin, China, is mainly composed of quartz (78.4%), feldspar (4.7%), clays (5.45%), and calcite (5.2%) with a small amount of other interstitial fillings. The elastic moduli of the matrix materials (40.32, 40.69 GPa) are estimated by computing the Voigt–Reuss–Hill average, and the density of the matrix materials is inverse calculated from sample density and porosity, i.e., $\rho_s = \rho/(1-\phi)$. Because the mineral composition of samples is known, several theoretical models can be used to calculate its composite intrinsic thermal conductivity, specific heat, and thermal expansion from the tables of values for minerals (Robertson 1988). Here, we choose the parallel model in Eq. (16) below to give the conductivity, specific heat, and thermal expansion of dry sandstone by

$$k^s = \sum_i f_i k_i^s, C_E^s = \sum_i f_i C_{Ei}^s, \text{ and } \alpha_s = \sum_i f_i \alpha_i^s, \tag{16}$$

where k_i^s, C_{Ei}^s, and α_i^s are the conductivity, specific heat, and thermal expansion of the i-th component of the rock and f_i is the corresponding weight fraction. To simplify, we assume that the effects of temperature and pressure on the thermal characteristics of the matrix are negligible. As shown in Table 2, we used Eq. (16) to obtain the thermophysical properties of solid phase at ambient conditions. It is worth noting that although the thermal expansion of pure mineral grains undergoing linear increases with temperature (Huotari and Kukkonen 2004), laboratory observation data from dry sandstone samples indicate that the thermal expansion coefficient of the rock matrix remains

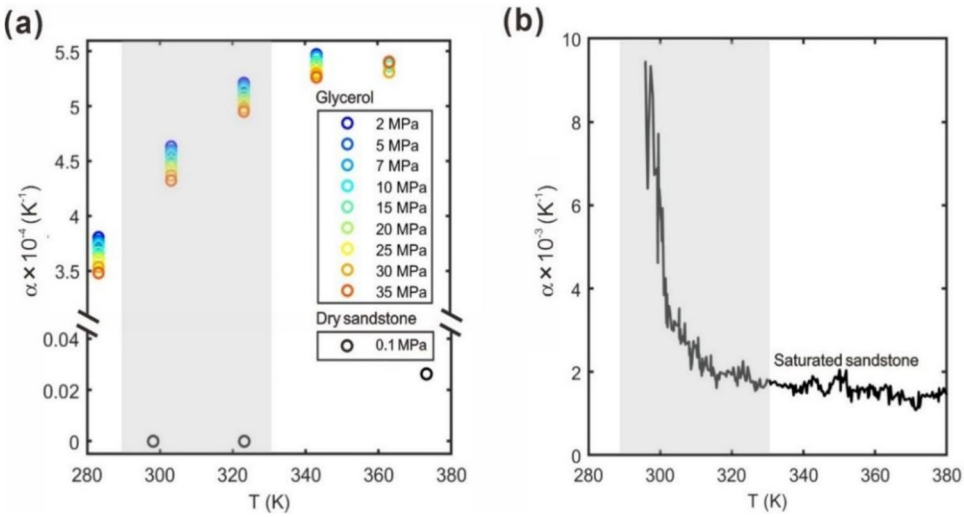

Fig. 8 Thermal expansion coefficient of glycerol as a function of pressure and temperature calculated from GMA EoS (**a**, Prieto et al. 2016), dry (**a**, Sirdesai et al. 2018) and saturated (**b**, Xiao et al. 2024) sandstones measured under varying temperature and atmospheric pressure

Table 3 Physical properties of glycerol as a function of temperature

Pore fluid at 1 MPa	T (K)[a]	$\eta(10^{-3}$ Pa·s)[a]	K_f (GPa)[a]	ρ_f(kg/m^2)[a]	c_f (×10^6 kg/(m·s^2·K))[b]
Glycerol	296.15	1410	4.66	1261.3	2.71
	313.15	284	4.36	1248.9	2.75
	333.15	81.3	4.15	1235.1	2.83

[a]Yin et al. (2017)

[b]Ahmadi et al., (2023)

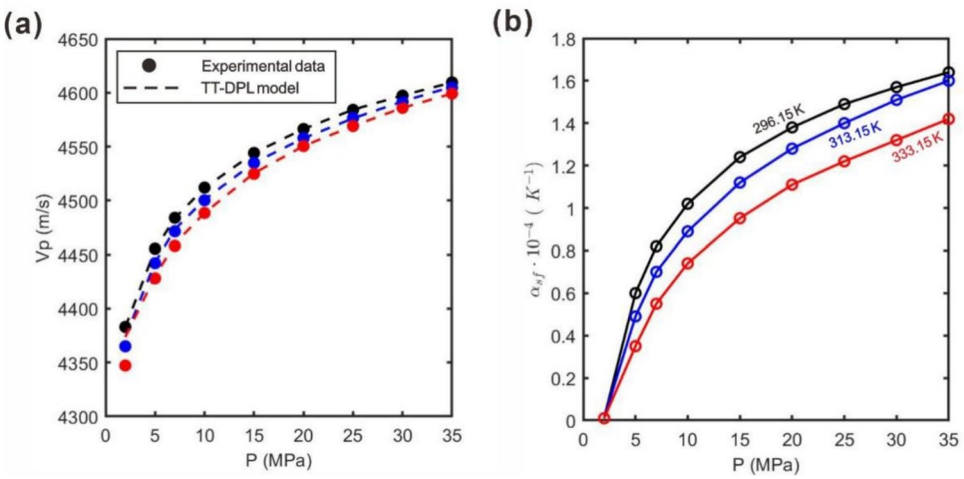

Fig. 9 Predicted and measured ultrasonic P wave velocities of the glycerol-saturated sandstone as a function of pressure

zero below 100 °C with the mismatch of the coefficients of thermal expansion between adjacent grains and varying porosity (Fig. 8a; Sirdesai et al. 2018). Therefore, we do not consider the temperature and pressure dependence of solid thermal expansion, and set the value as a constant in Eq. (16). In addition, as pore fluids, most properties of glycerin show strong dependence on temperature, but little sensitivity to pressure, such as viscosity, specific heat bulk modulus, and density, as presented in Table 3. We estimated the glycerin thermal expansion coefficients combined with selected values from the literature covering the ranges of $T = (278–373)$ K and of $P = (0.1–200)$ MPa, fitted using the Goharshadi–Morsali–Abbaspour equation of state (GMA EoS) (Fig. 8a; Goharshadi et al. 2005). As shown in Fig. 8b, the coefficient of saturated sandstone significantly decreases with temperature (Xiao et al. 2024), which contradicts the fluid thermal expansion coefficient in the temperature range of 296.15–333.15 K. Therefore, an increase in temperature

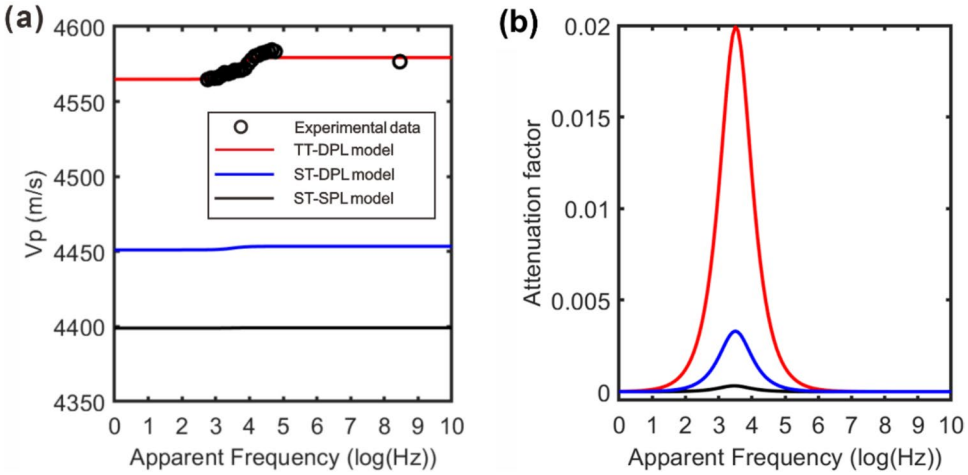

Fig. 10 Measured ultrasonic P wave velocity of glycerol-saturated sandstone at 40 °C and 20 MPa (black circles), phase velocity and attenuation as functions of frequency, predicted by the TT-DPL (red solid line), ST-DPL (blue solid line), and ST-SPL (black solid line) thermoporoelasticity models, respectively

causes the solid–fluid coupled thermal expansion coefficient to decrease, while an increase in pressure results in a closer coupling between the solid and fluid phases, leading to an increase in the solid–fluid coupled thermal expansion coefficient. As the solid–fluid coupled thermal expansion coefficient has not been accurately measured or reported, it is treated as an undetermined parameter in the TT-DPL model, and the aforementioned trend of α_{sf} variation with temperature and pressure has been confirmed in subsequent parameter inversion (Fig. 9b).

Similar to the previous plane wave analysis method, the velocity dispersion curve of the TT-DPL is obtained by solving the characteristic Eq. (13), and then compared with experimental data to calculate the relative error. The nonlinear least squares optimization algorithm is then applied to iteratively optimize the unknown parameters. Figure 10a shows the theoretical predictions under glycerol-saturated conditions (dashed lines), which agree with experimental measurements. As is expected, the inverted value of α_{sf} which intuitively reflects the characteristic that the solid–fluid coupling effect increases with decreasing temperture and increasing pressure in the ranges of $T = (296.15–333.15)$ K and $P = (2–35)$ MPa (Fig. 9b). At the same time, the inverted coefficient of thermal expansion of the material is consistent with the actual saturated rock properties, although the inverted α_f is one order of magnitude lower than the theoretical $\alpha_{glycerol}$ values from the GMA EoS. The cause of this error is that the fluid in the experimental data might not be pure glycerol. As mentioned in Yin et al. (2017), localized high pressure and dead volume during the rock sample saturation process can result in the mixing of glycerol with some air.

We compare the frequency-dependent velocities of the glycerin-saturated tight sandstone under conditions of 40°C and 20 MPa, using the TT-DPL, ST-DPL, and ST-SPL thermoporoelasticity models with and without the effect of solid–fluid thermal expansion, as well as with a partial effect. The thermal expansion coefficient, obtained through inversion in Fig. 9b, as a direct parameter (for TT-DPL and ST-DPL) or as an indirect parameter (calculating the thermal stress coefficient in ST-SPL as shown in Appendix A), is input into the models. Plane wave analyses are performed for a comprehensive comparison of dispersion and attenuation between the different thermoporoelasticity models as shown in Fig. 10. The TT-DPL model including the effect of solid–fluid thermal expansion shows a higher thermal attenuation and larger velocity dispersion both in seismic and high frequencies. Especially under typical rock parameter conditions, as discussed in Fig. 1, it is difficult to observe high frequency dispersion or even seismic frequency in the traditional thermoporoelasticity models. However, the TT-DPL model in Fig. 10b gives attenuation values about 0.02 that are common for laboratory measurements (Wei 2021). A large number of studies have reported the influence of thermal physical parameters and temperature on wave velocity (Wei et al. 2020; Hou et al. 2021; Li et al. 2022). Ignoring the effect of solid–fluid thermal expansion when fitting the data, however, leads to relatively high and incorrect values for the thermal conductivity, thermal relaxation time, and an abnormal temperature-dependent wave velocity trend.

4 Conclusions

Differences in temperature and thermophysical properties between the solid frame and the pore infill (fluid) lead to strong thermal coupling effects on microscopic interactions in the heat transfer process of porous rocks, resulting in significant influences on the dissipation and attenuation of elastic waves. We propose an analytical solution based on the TT-DPL model in this study to approach this issue that remains unexplored theoretically as far as known. The effect of solid–fluid thermal expansion is included in the derivation of the solution. Plane

wave analyses are performed for a comprehensive comparison of dispersion and attenuation between the TT-DPL, ST-DPL, and ST-SPL thermoporoelasticity models. The TT-DPL model accounts for the effect of solid–fluid thermal coupling and shows the larger thermal attenuation and velocity dispersion than the other two models. The physics of wave propagation is analyzed in detail for two different sets of thermoelastic properties, and the velocities and attenuation factors of the different wave modes are determined under different conditions. The simulations show the TT-DPL model gives reasonable attenuation values under typical rock properties.

We apply the TT-DPL model to interpret laboratory measurements on saturated sandstone with glycerin at varying temperatures and pressures. The inverted coefficient of solid–fluid thermal expansion, ranging from 1×10^{-7} K^{-1} to 1.6×10^{-4} K^{-1} in glycerol-saturated sandstone at $T=(296.15–333.15)$ K and $P=(2–35)$ MPa, reveals a closer interaction between the phases and a higher heat transfer efficiency. Its maximum value is constrained by porosity and the different thermal expansion coefficients of each phase. When also including the thermal expansion effect in the fitting process, the obtained specific heat capacity is in the order of 10^6, which is generally consistent with the actual properties of the saturated rock. Soft crack/fracture porosity becomes important in low frequencies. The proposed TT-DPL thermoelastic model attempts to bridge rock internal thermoelastic parameters (solid thermal expansion, fluid thermal expansion, and solid–fluid thermal expansion) and direct laboratory measurements (velocities, and attenuations). It describes dramatic velocity changes due to the mismatch in the thermal expansion coefficient and the thermal coupling effect during the heating and pressurization process. The TT-DPL model has the potential to build a physical understanding of the heat transfer process between solid and fluid in ultradeep hydrocarbon exploration, geothermal recovery, and other applications involving temperature variations within fluids.

Appendix A

We consider the thermoporoelastic medium to be loaded with temperature and effective stress, where infinitesimal strains are sufficient to describe the medium's microscale finite deformations. In this case, we have

$$\sigma_{ij}^{(m)}=\frac{\partial\psi}{\partial e_{ij}}=2\mu e_{ij}+Pe_{kk}\delta_{ij}+(Q\epsilon+C\theta^{s}+D_1\theta^{f})\delta_{ij}, \quad (17)$$

$$\sigma^{(f)}=\frac{\partial\psi}{\partial\epsilon}=Qe_{kk}+R\epsilon+D_2\theta^{f}+F\theta^{s}. \quad (18)$$

To obtain the elasticity coefficients in terms of known properties in Eqs. (17) and (18), we consider three ideal experiments, under static conditions (Biot and Willis 1957). First, the material is subjected to a pure shear deformation (e_{kk}=$\epsilon=0$). In this case, it is clear that μ is the shear modulus of the frame, since the fluid does not contribute to the shearing force. In the second ideal experiment, the material is enclosed in a thin, impermeable, flexible jacket and then subjected to an external hydrostatic pressure p. The pressure of the fluid inside the jacket remains constant, because the interior of the jacket is exposed to the atmosphere by a tube. The pore pressure remains essentially constant and $\sigma=0$. Only the skeleton affects the rock deformation. Then $\sigma_{ij}^{(m)}=-p\delta_{ij}$ and $e_{kk}=-p/K_b$, where K_b is the frame modulus. Substituting these relations into Eqs. (17) and (18), we obtain

$$P-\frac{Q}{R}=K_m. \quad (19)$$

In the third ideal experiment, the sample is immersed in the saturating fluid to which a pressure p is applied. The pressure acts both on the frame part $1-\phi$ and the fluid part ϕ of the surfaces of the sample.

$$\begin{aligned}1-\phi&=\frac{P}{K_s}+\frac{Q}{K_f},\\ \phi&=\frac{R}{K_f}+\frac{Q}{K_s}.\end{aligned} \quad (20)$$

Solving Eqs. (19) and (20), we obtain

$$\begin{aligned}P&=\frac{(1-\phi)\left(1-\phi-\frac{K_m}{K_s}\right)K_s+\phi\frac{K_s}{K_f}K_m}{1-\phi-K_m/K_s+\phi K_s/K_f}=\lambda+M(\alpha-\phi)^2,\\ Q&=\frac{\left(1-\phi-\frac{K_m}{K_s}\right)\phi K_s}{1-\phi-K_m/K_s+\phi K_s/K_f}=\phi(\alpha-\phi)M,\\ R&=\frac{\phi^2K_s}{1-\phi-K_m/K_s+\phi K_s/K_f}=\phi^2M,\end{aligned} \quad (21)$$

where α and M are the stiffness coefficients consistent with the Biot's notation related to solid bulk moduli K_s, fluid bulk moduli K_f, and porosity ϕ (Biot 1956; Carcione et al. 2019), $M=K_s/(1-\phi-K_m/K_s+\phi K_s/K_f)$, $\alpha=1-K_m/K_s$, and $K_m=\lambda+\frac{2}{3}\mu$.

To obtain the thermoelasticity coefficient in terms of the linear thermal expansion coefficient that can be measured in the laboratory experiments, let β_{ij} be the thermoelasticity coefficient of stress:

$$\begin{aligned}\beta_{ij}^{s}&=-\frac{1}{T_0}\frac{\partial^2\psi}{\partial e_{ii}\partial\theta^{*s}}=-\frac{\partial^2\psi}{\partial e_{ii}\partial\theta^{s}}=-C=\beta_s\delta_{ij},\\ \beta_{ij}^{f}&=-\frac{1}{T_0}\frac{\partial^2\psi}{\partial\epsilon\partial\theta^{*f}}=-\frac{\partial^2\psi}{\partial\epsilon\partial\theta^{f}}=-D_2=\beta_f\delta_{ij},\\ \beta_{ij}^{sf}&=-\frac{1}{T_0}\frac{\partial^2\psi}{\partial e_{ii}\partial\theta^{*f}}=-\frac{\partial^2\psi}{\partial e_{ii}\partial\theta^{f}}=-D_1=\beta_{sf}\delta_{ij},\\ \beta_{ij}^{fs}&=-\frac{1}{T_0}\frac{\partial^2\psi}{\partial\epsilon\partial\theta^{*s}}=-\frac{\partial^2\psi}{\partial\epsilon\partial\theta^{s}}=-F=\beta_{fs}\delta_{ij},\end{aligned} \quad (22)$$

in which case we have

$$e_{ii} = \frac{\phi^2 M\sigma_{ii}^{(m)} - 3\phi(\alpha-\phi)M\sigma^{(f)} + 3[\phi^2 M\beta_s - \phi(\alpha-\phi)M\beta_{fs}]\theta^s + 3[\phi^2 M\beta_{sf} - \phi(\alpha-\phi)M\beta_f]\theta^f}{2\mu + 3\lambda_c} \tag{23}$$

$$\epsilon = \frac{\phi(\phi-\alpha)M\sigma_{ii}^{(m)} + [2\mu+3\lambda+3M(\alpha-\phi)]\sigma^{(f)} + \left[(2\mu+3\lambda+3M(\alpha-\phi))\beta_f - 3\phi(\alpha-\phi)M\beta_{sf}\right]\theta^f + \left[(2\mu+3\lambda+3M(\alpha-\phi))\beta_{fs} - 3\phi(\alpha-\phi)M\beta_s\right]\theta^s}{2\mu+3\lambda_c}. \tag{24}$$

We replace the dilatation in the stress–strain relations in Eqs. (17) and (18) by Eqs. (23) and (24), and after some manipulations we get the corresponding displacement:

$$e_{ij} = \frac{\sigma_{ij}}{2\mu} - \frac{\lambda_c\phi^2 M\sigma_{ii}^{(m)}\delta_{ij}}{2\mu(2\mu+3\lambda_c)} - \frac{\phi M(\alpha-\phi)}{2\mu+3\lambda_c}\sigma^{(f)}\delta_{ij} + \frac{\phi^2 M\beta_{sf} - \phi M(\alpha-\phi)\beta_f}{2\mu+3\lambda_c}\theta^f\delta_{ij} + \frac{\phi^2 M\beta_s - \phi M(\alpha-\phi)\beta_{fs}}{2\mu+3\lambda_c}\theta^s\delta_{ij}. \tag{25}$$

$$\epsilon = \frac{\phi(\phi-\alpha)M\sigma_{ii}^{(m)}}{2\mu+3\lambda_c} + \frac{\left[2\mu+3\lambda_c+3M(\alpha-\phi)\right]\sigma^{(f)}}{2\mu+3\lambda_c} + \frac{\left[2\mu+3\lambda_c+3M(\alpha-\phi)\right]\beta_f - 3\phi M(\alpha-\phi)\beta_{sf}}{2\mu+3\lambda_c}\theta^f + \frac{\left[2\mu+3\lambda_c+3M(\alpha-\phi)\right]\beta_{fs} - 3\phi M(\alpha-\phi)\beta_s}{2\mu+3\lambda_c}\theta^s. \tag{26}$$

We define the linear coefficient of thermal expansion α_{ij} as

$$\alpha_{ij} = \frac{\partial\varepsilon}{\partial\theta} = f\left(\beta_{ij}, M^*\right). \tag{27}$$

In other words, α_{ij} represents the increase in strain per unit of temperature rise and is a function of the coefficient of thermoelasticity and the modulus; the unit is K^{-1}, not cm^3/g in Singh (2011). The thermoelasticity coefficient β_{ij} is the combination of the coefficient of thermal expansion multiplied by the modulus; the unit is $kg/(m{\cdot}s^2{\cdot}K)$ which is consistent with Carcione et al.'s (2019) study. Substituting Eqs. (25) and (26) into (27) to calculate the partial derivatives of the temperature difference of solids and fluids, respectively, we have

$$\alpha_{ij}^s = \frac{\partial e_{ij}}{\partial\theta^s} = \frac{\phi^2 M\beta_s - \phi M(\alpha-\phi)\beta_{fs}}{2\mu+3\lambda_c}\delta_{ij} = \alpha_s\delta_{ij}, \alpha_{ij}^{sf} = \frac{\partial e_{ij}}{\partial\theta^f} = \frac{\phi^2 M\beta_{sf} - \phi M(\alpha-\phi)\beta_f}{2\mu+3\lambda_c}\delta_{ij} = \alpha_{sf}\delta_{ij},$$
$$\alpha_{ij}^{fs} = \frac{\partial\epsilon}{\partial\theta^s} = \frac{[2\mu+3\lambda+3M(\alpha-\phi)]\beta_{fs} - 3\phi M(\alpha-\phi)\beta_s}{2\mu+3\lambda_c} = \alpha_{fs}, \alpha_{ij}^f = \frac{\partial\epsilon}{\partial\theta^f} = \frac{[2\mu+3\lambda+3M(\alpha-\phi)]\beta_f - 3\phi M(\alpha-\phi)\beta_{sf}}{2\mu+3\lambda_c} = \alpha_f\delta_{ij}, \tag{28}$$

where α_s and α_f are the coefficients of the thermal expansion of the particular phases, α_{ij}^{sf} indicates the effect on solid strain as the fluid temperature increases, and α_{ij}^{fs} represents the effect on fluid strain with increaseing temperature of the solid phase. There are three clerical errors in the interpretation of the parameters of Youseef's (2017) Eqs. (40) and (41), which should be corrected to $\alpha^s = \frac{RR_{11}-QR_{21}}{\Delta}$, $\alpha^{sf} = \frac{PR_{12}-QR_{22}}{\Delta}$, $\alpha^{fs} = \frac{PR_{21}-3QR_{11}}{\Delta}$. As shown in Eq. (21), $P = \lambda_{Youseef} = \lambda + M(\alpha-\phi)^2$, Δ reduces to $2\mu+3\lambda$. If we neglect the thermal coupling effect between the solid–fluid phases but include the thermal term within each phase, the thermoelasticity coefficient reduces to $\beta_s = (2\mu+3P)\alpha_s + Q\alpha_f$, $\beta_f = 3Q\alpha_s + R\alpha_f$. It is worth mentioning that Noda (1990) gives $\beta_s = (2\mu+3P)\alpha_s + 3Q\alpha_f$, $\beta_f = 3Q\alpha_s + 3R\alpha_f$ in his Eq. (11). The behavior of these quantities is such that for $\phi = 0, K_m = K_s, \alpha = 0, \beta_m = 3K_s\alpha_m$, and $\beta_s = 0$. For $\phi = 1, K_m = 0, \alpha = 1, \beta_m = 0$, and $\beta_f = K_f\alpha_f$.

Appendix B

The constitutive equations of the theory of thermoporoelasticity involve the coupling of the stress components with the temperature field (Carcione et al. 2019; Wei et al. 2020; Hou et al. 2021; Li et al. 2022). The equations of the entropy density rate for solids and liquids per unit mass of aggregate are defined as

$$-\frac{\partial \psi}{\partial T^s} = \rho \eta^s = \beta_s e_{kk} + \beta_{fs}\varepsilon - 2G\theta^s - J\theta^f, \tag{28}$$

$$-\frac{\partial \psi}{\partial T^f} = \rho \eta^f = \beta_{sf} e_{kk} + \beta_f \varepsilon - 2H\theta^s - J\theta^f. \tag{29}$$

Next, we replace the dilatation by their representations Eqs. (24) and (25) to calculate the entropy of the solid phase, and after some manipulations, we rewrite Eq. (28) as

$$\begin{aligned}\rho \eta^s = {} & \gamma_s \sigma_{ii}^{(m)} + \gamma_{fs}\sigma^{(f)} + \left(3\alpha_s\beta_s + \alpha_{fs}\beta_{fs} - 2G\right)\theta^s \\ & + \left(3\alpha_s\beta_{sf} + \alpha_{fs}\beta_f - J\right)\theta^f.\end{aligned} \tag{30}$$

With the assumption of η^s is independent of the temperature of the fluid phase, the coefficient of the fluid temperature term is equal to zero, $3\alpha_s\beta_{sf} + \alpha_{fs}\beta_f - J = 0$. Note that the unit of the temperture coupling coefficient J is kg/(m·s^2·K^2).

Acknowledgements This work was supported in part by the National Natural Science Foundation of China under grant 42230803 and in part by the 111 Project "Deep–Superdeep Oil and Gas Geophysical Exploration" under grant B18055.

Author contribution Conceptualization: Li-Yun Fu, Nianqi Li. Data curation: Wubing Deng, José M. Carcione. Funding acquisition: Li-Yun Fu. Investigation: Wubing Deng. Methodology: Nianqi Li, Li-Yun Fu, José M. Carcione, Wubing Deng. Resources: Li-Yun Fu. Software: Nianqi Li, José M. Carcione, Wubing Deng. Supervision: Li-Yun Fu, José M. Carcione. Validation: Nianqi Li. Visualization: Li-Yun Fu.Writing - original draft: Nianqi Li. Writing - review & editing: Nianqi Li, Li-Yun Fu, José M. Carcione.

Funding The National Natural Science Foundation of China, 42230803, Li-Yun Fu, the 111 Project "Deep-Superdeep Oil and Gas Geophysical Exploration", B18055, Li-Yun Fu

Declarations

Conflict of Interest The authors declare that they have no known competing financial interests or personal relationships that could have appeared to influence the work reported in this paper.

References

Abdulagatova ZZ, Abdulagatov IM, Emirov SN (2010) Effect of pressure, temperature, and oil-saturation on the thermal conductivity of sandstone up to 250 MPa and 520 K. J Pet Sci Eng 73(1–2):141–155. https://doi.org/10.1016/j.petrol.2010.05.016

Ahmadi P, Chapoy A, Burgass R (2023) An investigation on the thermophysical properties of glycerol. J Chem Thermodyn 178:106975. https://doi.org/10.1016/j.jct.2022.106975

Al-Bazali T (2005) Experimenal study of the membrane behaviour of shale during interaction with water-based and oil-based muds. University of Texas, Austin, USA

Armstrong BH (1984) Models for thermoelastic attenuation of waves in heterogeneous solids. Geophysics 49:1032–1040. https://doi.org/10.1190/1.1441718

Ba J, Carcione JM, Nie JX (2011) Biot-rayleigh theory of wave propagation in double-porosity media. J Geophys Res 116:B06202. https://doi.org/10.1029/2010JB008185

Banks D (2012) An introduction to thermogeology: ground source heating and cooling. John Wiley & Sons, Hoboken

Batzle M, Wang Z (1992) Seismic properties of pore fluids. Geophysics 57(11):1396–1408. https://doi.org/10.1190/1.1443207

Batzle M, Hofmann R, Han DH (2006) Heavy oils—seismic properties. Lead Edge 25(6):750–756. https://doi.org/10.1190/1.2210074

Biot MA (1956) Theory of propagation of elastic waves in a saturated porous solid. I. Low-frequency range. J Acoust Soc Am 28:168–178. https://doi.org/10.1121/1.1908241

Biot MA (1962) Mechanics of deformation and acoustic propagation in porous media. J Appl Phys 33:1482–1498. https://doi.org/10.1063/1.1728759

Biot MA, Willis DG (1957) The elastic coefficients of the theory of consolidation. J Appl Mech. https://doi.org/10.1115/1.4011606

Boschi E (1973) A thermoviscoelastic model of the earthquake source mechanism. J Geophys Res 78:7733–7737. https://doi.org/10.1029/JB078i032p07733

Breede K, Dzebisashvili K, Liu X, Falcone G (2013) A systematic review of enhanced (or engineered) geothermal systems: past, present and future. Geoth, Energy 1(1):1–27. https://doi.org/10.1186/2195-9706-1-4

Carcione JM (2007) Wave fields in real media: wave propagation in anisotropic, anelastic, porous and electromagnetic media. Elsevier, Amsterdam

Carcione JM, Wang ZW, Ling W, Salusti E, Ba J, Fu L-Y (2018) Simulation of wave propagation in linear thermoelastic media. Geophysics 84:T1–T11. https://doi.org/10.1190/geo2018-0448.1

Carcione JM, Cavallini F, Wang E, Ba J, Fu L-Y (2019) Physics and simulation of wave propagation in linear thermoporoelastic media. J Geophys Res Solid Earth 124:8147–8166. https://doi.org/10.1029/2019JB017851

Cermak V, Bodri L, Rybach L, Buntebarth G (1990) Relationship between seismic velocity and heat production: comparison of two sets of data and test of validity. Earth Planet Sci Lett 99(1–2):48–57. https://doi.org/10.1016/0012-821x(90)90069-a

Chandrasekharaiah DS (1998) Hyperbolic thermoelasticity: a review of recent literature. Appl Mech Rev. https://doi.org/10.1115/1.3098984

Cheng S, Li Z, Ge X, Li J, Zhang Y, Liang X, Feng H (1990) In-situ measurements of the effective thermal conductivity of oil-sandstone samples under simulated conditions. High Temp-High Press (Int J Res U.k.) 22(6):0018–1544

Cheng YF, Fu L-Y, Hou WT, Carcione JM, Deng WB, Wang ZW (2024) Thermo-poroelastic AVO modeling of Olkaria geothermal reservoirs. Geoenergy Sci Eng 241:213166. https://doi.org/10.1016/j.geoen.2024.213166

Chicco J, Verdoya M, Giuli G, Invernizzi C (2019) Thermophysical properties and mineralogical composition of the Umbria-Marche carbonate succession (central Italy). https://doi.org/10.1130/2019.2542(02)

Chicco JM, Mandrone G (2022) How a sensitive analysis on the coupling geology and borehole heat exchanger characteristics can improve the efficiency and production of shallow geothermal plants. Heliyon. https://doi.org/10.1016/j.heliyon.2022.e09545

Clarke JR (1928) Density and thermal expansion of chemical compounds under atmospheric pressure. In: International Critical Tables. Vol. III.

Cui X, Wong LNY (2021) A 3D thermo-hydro-mechanical coupling model for enhanced geothermal systems. Int J Rock Mech Min Sci 143:104744. https://doi.org/10.1016/j.ijrmms.2021.104744

Goharshadi EK, Morsali A, Abbaspour M (2005) New regularities and an equation of state for liquids. Fluid Phase Equilib 230(1–2):170–175. https://doi.org/10.1016/j.fluid.2004.12.010

Gray AS, Uher C (1977) Thermal conductivity of mica at low temperatures. J Mater Sci 12(5):959–965. https://doi.org/10.1007/bf00540978

Han DH, Liu J, Baztle M (2008) Seismic properties of heavy oils: measured data. Lead Edge 27:1108–1115. https://doi.org/10.1190/1.2978972

Hou W, Fu L-Y, Carcione JM, Wang ZW, Wei J (2021) Simulation of thermoelastic waves based on the Lord-Shulman theory. Geophysics 86(3):T155–T164. https://doi.org/10.1190/geo2020-0515.1

Hou W, Fu L-Y, Carcione JM (2023) Reflection and transmission of inhomogeneous plane waves in thermoporoelastic media. Surv Geophys 44:1897–1917. https://doi.org/10.1007/s10712-023-09782-z

Hou W, Fu LY, Carcione JM (2024) Reflection, transmission, and AVO response of inhomogeneous plane waves in thermoporoelastic media with two-temperature equations of heat conduction. Geophysics 89(5):MR297–MR307. https://doi.org/10.1190/geo2023-0625.1

Huotari T, Kukkonen I (2004) Thermal expansion properties of rocks: Literature survey and estimation of thermal expansion coefficient for Olkiluoto mica gneiss. Posiva Oy Olkiluoto Work Rep 4:62

Jacquey AB, Cacace M, Blöcher G, Scheck-Wenderoth M (2015) Numerical investigation of thermoelastic effects on fault slip tendency during injection and production of geothermal fluids. Energy Proc 76:311–320. https://doi.org/10.1016/j.egypro.2015.07.868

Jian SK, Fu L-Y, Liao ZH, Deng WB, Du QZ (2022) Elastic characteristics of fault damage zones within superdeep carbonates in Tarim Basin, Northwest China. J Geophys Eng 19(4):650–662. https://doi.org/10.1093/jge/gxac040

Kaminski W (1990) Hyperbolic heat conduction equation for materials with a nonhomogeneous inner structure. J Heat Transf. https://doi.org/10.1115/1.2910422

Kirby RK (1969) Thermal expansion of ceramics. Mechanical and thermal properties of ceramics. Oxford Academic, Oxford, pp 41–61

Kumar R, Vohra R, Gorla MG (2017) Variational principle and plane wave propagation in thermoelastic medium with double porosity under Lord-Shulman theory. J Solid Mech 9(2):423–433

Kumar M, Liu X, Kumari M, Yadav P (2022) Wave propagation at the welded interface of an elastic solid and unsaturated poro-thermoelastic solid. Int J Numer Methods Heat Fluid Flow 32:3526–3550. https://doi.org/10.1108/HFF-01-2022-0008

Kumar M, Bhagwan J, Kaswan P, Liu X, Kumari M (2023) Inhomogeneous waves propagation in double-porosity thermoelastic media. Int J Numer Methods Heat Fluid Flow 33:2927–2962. https://doi.org/10.1108/HFF-03-2023-0146

Kumar M, Priyanka L, Fu L-Y, Neelam K, Pradeep K, Li NQ (2024) Rayleigh-type wave in thermoporoelastic media with dual-phase-lag heat conduction. Int J Num Methods Heat Fsluid Flow. https://doi.org/10.1108/HFF-11-2024-0853

Li NQ, Fu L-Y, Yang J, Han T (2021) On three-stage temperature dependence of elastic wave velocities for rocks. J Geophys Eng 18:328–338. https://doi.org/10.1093/jge/gxab017

Li N, Deng W, Fu LY, Carcione JM, Han T (2022) Wave propagation in double-porosity thermoelastic media. Geophysics 87(6):MR265–MR277. https://doi.org/10.1190/geo2022-0008.1

Li NQ, Fu L-Y, Deng WB, Carcione JM, Yang J (2023) A thermo-hydromechanical model to evaluate the seismic properties of geothermal reservoirs. Geophysics 88(5):WB23–WB35. https://doi.org/10.1190/geo2022-0491.1

Liu F, Fu PC, Mellors RJ, Plummer MA, Ali ST, Reinisch EC, Liu Q, Feigl KL (2018) Inferring geothermal reservoir processes at the raft river geothermal field, Idaho, USA, through modeling InSAR-measured surface deformation. J Geophys Res Solid Earth 123(5):3645–3666. https://doi.org/10.1029/2017JB015223

Liu H, Dai G, Zhou F, Cao X (2022) A mixture theory analysis for reflection phenomenon of homogeneous plane-P1-wave at the boundary of unsaturated porothermoelastic media. Geophys J Int 228:1237–1259. https://doi.org/10.1093/gji/ggab379

Liu Y, Fu L-Y, Deng W, Hou W, Carcione JM, Wei J (2023) Simulation of wave propagation in thermoporoelastic media with dual-phase-lag heat conduction. J Therm Stress 46(7):620–638. https://doi.org/10.1080/01495739.2023.2193225

Li-Yun F (2017) Deep-Superdeep Oil & Gas Geophysical Exploration 111. Program report jointly initiated by MOE and SAFEA, B18055. School of Geosciences China University of Petroleum (East China), Beijing

Li-Yun F (2019) Geophysical characterization of Olkaria geothermal reservoirs in Kenya. Tech Report, BGPYJY2017-963. CNPC Greatwall Drilling Company, Beijing

Lord H, Shulman Y (1967) A generalized dynamical theory of thermoelasticity. J Mech Phys Solids 15:299–309. https://doi.org/10.1016/0022-5096(67)90024-5

Ma Z, Zhang G, Gamage RP, Zhang C (2021) Measurement of thermal expansion coefficient of rock minerals using XRD and its implications to thermal damage mechanism. IOP Conf Ser Earth Environ Sci 861(7):072021. https://doi.org/10.1088/1755-1315/861/7/072021

Maqsood A, Kamran K (2005) Thermophysical properties of porous sandstones: measurements and comparative study of some representative thermal conductivity models. Int J Thermophys 26:1617–1632. https://doi.org/10.1007/s10765-005-8108-3

Mitra K, Kumar S, Vedevarz A, Moallemi MK (1995) Experimental evidence of hyperbolic heat conduction in processed meat. J Heat Transfer. https://doi.org/10.1115/1.2822615

Morozov IB, Deng W (2016) Macroscopic framework for viscoelasticity, poroelasticity, and wave-induced fluid flows—Part 1: general linear solid. Geophysics 81(1):L1–L13. https://doi.org/10.1190/geo2014-0171.1

Nava R, Amorer L, Pereira D (1994) Viscoelastic relaxation at megahertz frequencies in a Guasare (Venezuela) coal. Fuel 73(1):51–55. https://doi.org/10.1016/0016-2361(94)90187-2

Nield DA, Bejan A (2006) Convection in porous media, vol 3. Springer, Berlin

Noda N (1990) Thermal stress problem in a fluid-filled porous circular cylinder. ZAMM Z Angew Math Mech 70:543–549. https://doi.org/10.1002/zamm.19900701203

Oetting FL, Holley CE (1982) The specific heat capacity of biotite. J Chem Thermodyn 14(11):1029–1034. https://doi.org/10.1016/0021-9614(82)90145-8

Olasolo P, Juárez MC, Morales MP, Liarte IA (2016) Enhanced geothermal systems (EGS): a review. Renew Sustain Energy Rev 56:133–144. https://doi.org/10.1016/j.rser.2015.11.031

Poletto F, Farina B, Carcione JM (2018) Sensitivity of seismic properties to temperature variations in a geothermal reservoir. Geothermics 76:149–163. https://doi.org/10.1016/j.geothermics.2018.07.001

Prieto NM, Souza TA, Egas AP, Ferreira AG, Lobo LQ, Portugal AT (2016) Liquid glycerol: experimental densities at pressures of up to 25 MPa, and some derived thermodynamic properties. J Chem Thermodyn 101:64–77. https://doi.org/10.1016/j.jct.2016.05.006

Rabbani A, Schmitt DR (2018) Ultrasonic shear wave reflectometry applied to the determination of the shear moduli and viscosity of a viscoelastic bitumen. Fuel 232:506–518. https://doi.org/10.1016/j.fuel.2018.05.175

Richter D, Simmons G (1974) Thermal expansion behavior of igneous rocks. Int J Rock Mech Mining Sci Geomech Abstr 11(10):403–411. https://doi.org/10.1016/0148-9062(74)91111-5

Ritsema J, Deuss AA, Van Heijst HJ, Woodhouse JH (2011) S40RTS: a degree-40 shear-velocity model for the mantle from new Rayleigh wave dispersion, teleseismic traveltime and normal-mode splitting function measurements. Geophys J Int 184(3):1223–1236. https://doi.org/10.1111/j.1365-246x.2010.04884.x

Robertson EC (1988) Thermal properties of rocks (No. 88-441). US Geological Survey, Reston

Roshan H, Andersen MS, Acworth RI (2015) Effect of solid–fluid thermal expansion on thermo-osmotic tests: an experimental and analytical study. J Pet Sci Eng 126:222–230. https://doi.org/10.1016/j.petrol.2014.12.005

Rudgers AJ (1990) Analysis of thermoacoustic wave propagation in elastic media. J Acoust Soc Am 88(2):1078–1094. https://doi.org/10.1121/1.399856

Savage J (1966) Thermoelastic attenuation of elastic waves by cracks. J Geophys Res 71:3929–3938. https://doi.org/10.1029/jz071i016p03929

Schmitt DR (1999) Seismic attributes for monitoring of a shallow heated heavy oil reservoir: a case study. Geophysics 64:368–377. https://doi.org/10.1190/1.1444541

Sharma MD (2008) Wave propagation in thermoelastic saturated porous medium. J Earth Syst Sci 117:951–958. https://doi.org/10.1007/s12040-008-0080-4

Simmons NA, Forte AM, Boschi L, Grand SP (2010) GyPSuM: A joint tomographic model of mantle density and seismic wave speeds. J Geophys Res 115:B12310. https://doi.org/10.1029/2010JB007631

Singh B (2011) On propagation of plane waves in generalized porothermoelasticity. Bull Seismol Soc Am 101(2):756–762. https://doi.org/10.1785/0120100091

Sirdesai NN, Singh A, Sharma LK, Singh R, Singh TN (2018) Determination of thermal damage in rock specimen using intelligent techniques. Eng Geol 239:179–194. https://doi.org/10.1016/j.enggeo.2018.03.027

Skinner BJ (1966) Thermal expansion. Handbook of physical constants, vol 97. Oxford Academic, Oxford, pp 75–96

Soler JM (2001) The effect of coupled transport phenomena in the Opalinus Clay and implications for radionuclide transport. J Contam Hydrol 53(1–2):63–84. https://doi.org/10.1016/S0169-7722(01)00140-1

Spencer JW (2013) Viscoelasticity of Ells River bitumen sand and 4D monitoring of thermal enhanced oil recovery processes. Geophysics 78(6):D419–D428. https://doi.org/10.1190/geo2012-0535.1

Treitel S (1959) On the attenuation of small-amplitude plane stress waves in a thermoelastic solid. J Geophys Res 64:661–665. https://doi.org/10.1029/jz064i006p00661

Tura A, Lumley DE (1998) Subsurface fluid flow properties from time-lapse elastic wave reflection data. Math Method Geophys Imaging V 3453:125–138. https://doi.org/10.1117/12.323284

Tzou DY (1995) Experimental support for the lagging behavior in heat propagation. J Thermophys Heat Transf 9(4):686–693. https://doi.org/10.2514/3.725

Vedavarz A, Mitra K, Kumar S, Moallemi MK (1992) Effect of hyperbolic conduction on temperature distribution in laser irradiated tissue with blood perfusion. Winter annual meeting of the American society of mechanical engineers. ASME, New York, pp 7–16

Wang ZW, Fu L-Y, Wei J, Hou W, Ba J, Carcione JM (2020) On the green function of the Lord-Shulman thermoelasticity equations. Geophys J Int 220:393–403. https://doi.org/10.1093/gji/ggz453

Wang E, Carcione JM, Yuan Y, Ba J (2021) Reflection of inhomogeneous plane waves at the surface of a thermo-poroelastic medium. Geophys J Int 224:1621–1639. https://doi.org/10.1093/gji/ggaa543

Wang ZW, Fu L-Y, Jian SK, Deng WB (2023) Application of a model-driven simultaneous prestack inversion of rock physical properties in ultra-deep Ordovician carbonate reservoirs in the Shunbei area. Front Earth Sci 10:1035735. https://doi.org/10.3389/feart.2022.1035735

Wei J, Fu L-Y, Wang ZW, Ba J, Carcione JM (2020) Green's function of the Lord-Shulman thermoporoelasticity theory. Geophys J Int 221:1765–1776. https://doi.org/10.1093/gji/ggaa100

Wei, Q. 2021 Effects of rock and fluid properties on seismic dispersion and attenuation in sandstone. In: Doctoral dissertation.

Wong TF, Brace WF (1979) Thermal expansion of rocks: some measurements at high pressure. Tectonophysics 57(2–4):95–117. https://doi.org/10.1016/0040-1951(79)90143-4

Xiao W, Zhang D, Luo W, Huang Y, Wan H, Li S (2024) Influence of temperature on building sandstone: insights from microstructure, thermal strain and rupture crack. Constr Build Mater 451:138888. https://doi.org/10.1016/j.conbuildmat.2024.138888

Yang J, Fu L-Y, Han TC, Deng WB, Fu BY (2025) Thermoacoustoelasticity for elastic wave propagation in preheated and prestressed solid rocks. Rock Mech Rock Eng. https://doi.org/10.1007/s00603-024-04361-z

Yin H, Zhao J, Tang G, Zhao L, Ma X, Wang S (2017) Pressure and fluid effect on frequency-dependent elastic moduli in fully saturated tight sandstone. J Geophys Res Solid Earth 122(11):8925–8942. https://doi.org/10.1002/2017JB014244

Youssef HM (2007) Theory of generalized porothermoelasticity. Int J Rock Mech Min Sci 44(2):222–227. https://doi.org/10.1016/j.ijrmms.2006.07.001

Yuan H, Han DH, Zhao L, Huang Q, Zhang W (2019) Attenuation analysis of heavy oil sands based on laboratory measurements. Geophysics 84(5):B299–B309. https://doi.org/10.1190/geo2018-0171.1

Tzou D Y. Macro-to microscale heat transfer: the lagging behavior[M]. John Wiley & Sons, 2014.

Terms and Conditions

Springer Nature journal content, brought to you courtesy of Springer Nature Customer Service Center GmbH (“Springer Nature”).
Springer Nature supports a reasonable amount of sharing of research papers by authors, subscribers and authorised users (“Users”), for small-scale personal, non-commercial use provided that all copyright, trade and service marks and other proprietary notices are maintained. By accessing, sharing, receiving or otherwise using the Springer Nature journal content you agree to these terms of use (“Terms”). For these purposes, Springer Nature considers academic use (by researchers and students) to be non-commercial.
These Terms are supplementary and will apply in addition to any applicable website terms and conditions, a relevant site licence or a personal subscription. These Terms will prevail over any conflict or ambiguity with regards to the relevant terms, a site licence or a personal subscription (to the extent of the conflict or ambiguity only). For Creative Commons-licensed articles, the terms of the Creative Commons license used will apply.
We collect and use personal data to provide access to the Springer Nature journal content. We may also use these personal data internally within ResearchGate and Springer Nature and as agreed share it, in an anonymised way, for purposes of tracking, analysis and reporting. We will not otherwise disclose your personal data outside the ResearchGate or the Springer Nature group of companies unless we have your permission as detailed in the Privacy Policy.
While Users may use the Springer Nature journal content for small scale, personal non-commercial use, it is important to note that Users may not:

1. use such content for the purpose of providing other users with access on a regular or large scale basis or as a means to circumvent access control;
2. use such content where to do so would be considered a criminal or statutory offence in any jurisdiction, or gives rise to civil liability, or is otherwise unlawful;
3. falsely or misleadingly imply or suggest endorsement, approval , sponsorship, or association unless explicitly agreed to by Springer Nature in writing;
4. use bots or other automated methods to access the content or redirect messages
5. override any security feature or exclusionary protocol; or
6. share the content in order to create substitute for Springer Nature products or services or a systematic database of Springer Nature journal content.

In line with the restriction against commercial use, Springer Nature does not permit the creation of a product or service that creates revenue, royalties, rent or income from our content or its inclusion as part of a paid for service or for other commercial gain. Springer Nature journal content cannot be used for inter-library loans and librarians may not upload Springer Nature journal content on a large scale into their, or any other, institutional repository.
These terms of use are reviewed regularly and may be amended at any time. Springer Nature is not obligated to publish any information or content on this website and may remove it or features or functionality at our sole discretion, at any time with or without notice. Springer Nature may revoke this licence to you at any time and remove access to any copies of the Springer Nature journal content which have been saved.
To the fullest extent permitted by law, Springer Nature makes no warranties, representations or guarantees to Users, either express or implied with respect to the Springer nature journal content and all parties disclaim and waive any implied warranties or warranties imposed by law, including merchantability or fitness for any particular purpose.
Please note that these rights do not automatically extend to content, data or other material published by Springer Nature that may be licensed from third parties.
If you would like to use or distribute our Springer Nature journal content to a wider audience or on a regular basis or in any other manner not expressly permitted by these Terms, please contact Springer Nature at

onlineservice@springernature.com